Corresponding Author: Dr. T. H. New,

Corresponding Author's Institution: Nanyang Technological University

First Author: J. L. Heng

Order of Authors: J. L. Heng; T. H. New; P. A. Wilson

Abstract: In this paper, an Eulerian granular numerical model is applied in the modelling of an industrial scale pneumatic-based cement conveying system. Steady-state simulation results are found to match pressure and outlet flowrate values with actual system data. By modifying the inlet pressure and material feed rate, data that predicts the performance of the conveying system have been obtained within the present study. Transient simulations have also been conducted and the results reveal intricate details of the cement flows along the pneumatic pipes and pipe bends. In particular, particle roping behaviour is observed to follow the sides of the wall before, during and after the pipe bends. A sloshing-like cement flow motion is also observed after the cement exits the bend. The concentration distribution of the cement particles is found not only to be partly due to gravitational effects but also the pneumatic pipe configuration. Lastly, close inspection of the secondary flows within the pneumatic pipe shows that their directional changes lead to a corresponding change in the particle roping direction, indicating that particle roping is closely associated with the secondary flow structures induced by the exact pipe configuration.

Authors' responses to Reviewer #1 comments

The authors thank the reviewer for the constructive comments arising from the review of the manuscript. Below are point-by-point responses by the authors to the reviewers' comments:

Note: Revisions made to manuscript to address Reviewer #1 comments are highlighted in red.

1. **Reviewer's comment**: If d_s represents particle diameter in the appendix, what is d in Table 2 where Re_p is newly introduced. Then, what is Re_p and its denominator mu as mu_g is used in the Appendix but never defined. Where do you use Re_p in the simulation setup--it is not appeared in any of the equations in the manuscript.

   Author's response: The notations have been revised to be consistent with the text and appendix. Equations from Table 2 are relationships determined by previous researchers (refs. [10, 28]) that were used in the current work to calculate pressure drop across various pipe sections. These values are then compared against pressure values that were obtained in the simulations in the later part of the manuscript (Figure 5).

2. **Reviewer's comment**: What is the 'epsilon' in Table 2 in the expression for lambda_g. It should be a length scale, surface roughness I would guess, but it is NEVER defined in the manuscript. If I am correct, then PLEASE use another variable for that k-'epsilon' turbulence model.

   Author's response: The epsilon in Table 2 is indeed the surface roughness and this information has been added into Table 2. The notation has also been changed to epsilon_p to differentiate against rate of dissipation of turbulence energy in the k-epsilon turbulence model.

3. **Reviewer's comment**: Finally, line 37 on p.12: In my previous review, I added quotation mark to the "square" in the description line ---the square of the mean velocity. It was because I was very surprised about such a mistake. It is bizzare that the authors also included the quotation mark in their manuscript.

   Author's response: The authors have reviewed the previous concerns of the reviewer and the author's responses pertaining to this portion of the manuscript. The reviewer had initially suspected that the pressure drop across different pipe bends depends on the mean velocity. Hence, the authors attempted to address this by dividing absolute pressure values obtained from the simulations by the square of the mean velocity to show that $\Delta p = f(v^2)$. In the reviewer's second response, it was pointed out that concise statements should be used. That the revised statement should have read "divided by the square of the local mean velocity" instead of "divided by the mean velocity". In the current reviewer's response, the authors had initially thought that the word "square" was suggested to be wrongly used in the second revision.

   If the alternate interpretation of the authors is correct, the authors now realize that a miscommunication has occurred in the exchange. The reviewer had used quotation marks for the word square as a means of emphasizing that the word is missing, rather than an application of semiotics to highlight to the reader that $\Delta p = f(v^2)$. Hence, the authors do

not hereby attempt to replace the word square, instead opting to simply remove the quotations in hopes that the reviewer's concerns are now addressed.

4. **Reviewer's comment**: The equation numbers in the Appendix should be (25)(26) instead of (255)(266).

   Author's response: The labelling error has been rectified.

Application of an Eulerian granular numerical model to an industrial scale pneumatic conveying pipeline

J. Heng[1,2], T.H. New[1]* and P.A. Wilson[2]

[1] School of Mechanical and Aerospace Engineering, Nanyang Technological University

50 Nanyang Avenue, Singapore 639798, Singapore

[2] Faculty of Engineering and the Environment, University of Southampton, University Road,

Southampton SO17 1BJ, United Kingdom

Abstract

In this paper, an Eulerian granular numerical model is applied in the modelling of an industrial scale pneumatic-based cement conveying system. Steady-state simulation results are found to match pressure and outlet flowrate values with actual system data. By modifying the inlet pressure and material feed rate, data that predicts the performance of the conveying system have been obtained within the present study. Transient simulations have also been conducted and the results reveal intricate details of the cement flows along the pneumatic pipes and pipe bends. In particular, particle roping behaviour is observed to follow the sides of the wall before, during and after the pipe bends. A sloshing-like cement flow motion is also observed after the cement exits the bend. The concentration distribution of the cement particles is found not only to be partly due to gravitational effects but also the pneumatic pipe configuration. Lastly, close inspection of the secondary flows within the pneumatic pipe shows that their directional changes lead to a corresponding change in the particle roping direction, indicating that particle roping is closely associated with the secondary flow structures induced by the exact pipe configuration.

* Corresponding author: dthnew@ntu.edu.sg, Tel: +(65) 67905130

1 Introduction

Many industries transport bulk materials over extended distances using pneumatic conveying processes. Examples of which are the power generation industry for the transport of pulverized coal; food industry for the transport of powdery ingredients such as wheat, flour or sugar; and construction industry for the transport of cement powder. The application of pneumatic conveying comes from the many benefits that a pneumatic conveying system have over conventional belt conveying systems [1]. Numerical simulations have emerged over the years as an increasingly reliable and accurate method to study the mechanisms and performance of pneumatic conveying. Researchers had come up with many different numerical models catering to different conditions or area of interest in the flow. Apart from direct numerical simulations (DNS) and solving the complete equations of motion for each individual particle, there is no one unified model to use for gas-particle flows. In most cases, only the most appropriate modelling is being applied to reduce computational cost.

Numerical simulations had been used to study numerous aspects of pneumatic conveying. McGlinchey et al. [2] looked at the effects of an expanding pipe on the flow behaviour and identified the increased aeration of the abrupt expansion to be beneficial to the conveying process. Behera et al. [3] studied the inclusion of particle size variations in their numerical simulations of fine-particles conveying and observed good agreements between the pressure drop data between experiments and numerical simulations. They also found that segregation of different particle diameters happens in the pipeline, with different slip velocities for the bottom dense phase region and the top dilute phase region. In a study relevant to this paper, Ibrahim et al. [4] considered the effects of pipe bend orientation on pneumatic conveying flow behaviour. They looked at each orientation of the pipe bends individually and used numerical simulations to predict the particle trajectories. Schallert and Levy [5] performed an

2

investigation on the flow within a combination of pipe bends with different orientations. In particular, they studied the flow changes associated with a horizontal-to-horizontal pipe bend followed by a horizontal-to-vertical pipe bend. One interesting observation made in that study was that the material spiral along the vertical pipe wall after exiting the pipe bend. Examples of other applications of numerical simulation include investigation of pressure drop across pipe bends [6], deposition characteristics [7] and dune formations [8]. Such cases exhibit the ability of numerical simulations applied to study pneumatic conveying processes.

In designing a pneumatic pipeline, it will be highly desirable if favourable design aspects of experimental pipelines can be scaled-up directly. In the commonly cited pneumatic conveying design guide, Mills [1] provided procedures to scale up pipe length and diameters on the basis of similar pressure drop and air velocities. However, further research [9] has shown that they were far from perfect and further improvements could be made. Pan [10] and Mallick and Wypych [11] worked on trying to improve such scaling-up procedures. While the results were promising, the conclusions drawn were that the order of inaccuracy was only acceptable in practical design practice. When applying such techniques, a suitable numerical or theoretical model should be applied and more appropriate resulting scaling-up techniques have to be sought if better predictions are to be achieved. As such, the direct application of numerical simulation to the conveying pipeline appears to be a viable methodology to do that.

The purpose of this study is to look into the numerical simulation of a large full-scale industrial pneumatic-based cement conveying system currently in active operation. Firstly, important quantitative data such as the pressure drop and output capacity will be obtained directly from steady-state simulations, the results of which will bridge theoretical and practical applications to simplify pipeline designing procedures. Secondly, transient

3

simulations will be performed on a selected test case to illustrate and gain specific insights into the flow characteristics. In particular, particle concentrations within the pipe and secondary flow structures will be investigated to attain better understandings of the flow behaviour within the pipeline, which will not be available from the actual industrial system. Finally, conclusions will then be drawn from the results presented within the context of how computationally intensive numerical simulations such as the ones conducted here will benefit industrial applications.

2   Numerical procedure

2.1   Geometry

The geometry used in this numerical study is modelled directly after one of the pneumatic pipelines at Jurong Port Pte. Ltd. (JPPL) cement terminal. There are two pipelines that discharge into a single silo and they share the same dust collector system. As both pipelines are similar and they work independently of each other, only one of the pipeline will be studied. A perspective projection of the single pipeline that is studied here is shown in Figure 1. All straight pipe sections are orthogonal to each other as indicated by the coordinate system. Due to physical and operational constraints, it is not possible to obtain actual flow data along various sections of the pipeline as it cannot be modified or have measuring probes inserted. Therefore, a breakup of the computational domain into smaller sections is not possible - since the boundary conditions of the broken-up pipe sections cannot be defined. The pipeline consists of five 90° bends of bend radius 2.5m. Its inner diameter is 0.3556m (i.e. 14 inches) everywhere and the total pipe length (as measured along its axis) is 156.2m. Details on the various pipe section dimensions are provided in Figure 2 – note that the pipe diameter is not drawn to scale. The air mover back pressure at the inlet side is measured as 1.8bar. The maximum rated capacity of the dust collector system downstream of the pipe is

4

24,000m^3/h. The dust collector is running at maximum capacity and is being shared between two pipelines. Therefore, if both pipelines are assumed to be conveying at the same rate, this means that the maximum airflow that can be achieved in one of the pipelines can be reasonably assumed to be approximately 12,000m^3/h. Currently, only operational bulk flow data can be obtained by averaging throughout the entire conveying operation, that is, the throughput is averaged through time. When both pipes are working together, the system is able to convey cement at a rate of approximately 800*tonnes/hour* (*tph*) or 400*tph* for each pipeline. However, it is to be highlighted that these values are inclusive of the start-up/power-down phases and down times in between. The ideal flow rate is estimated to be about 500*tph* where the start-up/power-down and down times are excluded. The cement is discharged into a silo at the end of the conveying system that is at atmospheric pressure.

2.2 Governing equations

Following previous work [12], where the Eulerian granular model had been shown to capture cement flows reasonably well, this study will adopt the same model with changes to the solid phase material properties to fit the current cement conveying investigation. The Eulerian granular model has been adopted using Fluent (ANSYS Inc.). The model is a two-fluid model that treats both the gas and solid phase as continuums. The list of equations that are referenced within the text that follows can be found in the appendix.

In a two-phase flow, the idea of volume fraction is introduced. The model applies the continuum hypothesis for the solid phase. It assumes all the solid particles can be mathematically formulated like that of a fluid. The solids, together with the fluid, are then treated as two interpenetrating continuums. This interpenetrating effect is captured by a dimensionless variable called the volume fraction, α, where $0 \leq \alpha \leq 1$. In a certain (fixed)

5

space, the volume occupied by a certain phase q is the integral of the volume fraction multiplied by the volume.

For the current study, no mass exchange mechanisms are present between air and cement, and that the air does not gain or lose mass in other forms. Therefore, the right-hand sides of equations 1 and 4, where the mass source terms usually reside, are zero. Compared with the gas momentum conservation (equation 2), the additional terms $\overrightarrow{F_{td,s}}$ and $\overrightarrow{R_{gs}}$ on the right-hand side of the solid momentum conservation (equation 5) are due to interactions between different phases. As for equations 5 and 6, there are several unknowns that would require mathematical closure before the equations can be solved. Namely, the solids pressure p_s, sum of forces $\vec{F}$, sum of interphase momentum exchange $\vec{R}$, solids bulk viscosity λ_s and solids viscosity μ_s.

The solids pressure is an additional pressure term resulting from assuming the form of the stress tensor analogous to a Newtonian fluid. Similar to gas pressure, the solids pressure should in some way be related by a temperature term and volume term, since the pressure of an ideal gas depends on such factors ($pV = nRT$). Lun et al. [13] utilized a collisional particle pair-distribution function, which was obtained by simple kinetic analysis by Savage and Jeffrey [14], to derive the solids pressure p_s which consists of a kinetic part and a collisional part (equation 7). The coefficient of restitution for collision e_{ss} is taken as 0.9 in this study, following the conclusions of the work of Ehsani et al. [15]. The first term in the right-hand side of equation 7 represents the contributions from the kinetic part and the second term, from the collisional part. The interpretation of granular temperature is obvious. However, unlike in gases where the temperature is easily quantifiable, the granular temperature is proportional to the particles' fluctuation (equation 8).

6

Ding and Gidaspow [16] derived the transport equation for granular temperature (equation 9) where the diffusion coefficient k_{Θ_s} follows the work of Syamlal et al. [17] whom neglected the kinetic contribution from the expression by Lun et al. [13] as it tends to an unphysical value at low volume fractions. The collisional dissipation of energy γ_{Θ_s} is from the expression by Lun et al. [13] based on the assumption of slight inelasticity and the energy exchange between the phases is given by Gidaspow et al. [18].

What remains in the solids pressure and granular temperature formulation is the radial distribution function $g_{0,ss}$. The function is a correction factor to account for the changes in the probability of collision between two particles when the solid phase gets 'denser', i.e. the local solid phase volume fraction increases, resulting in higher possibilities of collision. Although not directly analogous, it can be argued that the radial distribution function serves the same purpose of the volume term in ideal gas theory. This function should then tend towards 1 and ∞ when the solid volume fraction tends towards 0 and the packing limit respectively. The radial distribution function $g_{0,ss}$ is presented by Ogawa et al. [19] through a kinetic model of collision of particles. For regular spheres of constant diameter, the packing limit is 0.63 [20].

The forces in the right hand side of equation 5 should include forces like the lift force $\vec{F}_{lift,s}$, wall lubrication force $\vec{F}_{wl,s}$, virtual mass force $\vec{F}_{vm,s}$, and/or turbulent dispersion force $\vec{F}_{td,s}$. As cement particles are small, with diameters in the order of $10^{-5}m$, the lift force on the cement particles is insignificant compared to the drag. Wall lubrication force is only pertinent to bubbly multiphase flows and virtual mass force is appropriate only when the density of the secondary phase is much lesser than that of the primary phase. This leaves the reduced solid

phase momentum equation to take the form shown in equation 5. The turbulent dispersion force $\vec{F}_{td,s}$ is modelled with the Favre-averaged drag (FAD) model [21] that is included in the software. Two other models, namely the Simonin model [22] and Lopez de Bertodano model [23] are available. The Simonin model essentially estimates the dispersion scalar D_s in equation 13 by the turbulent viscosity, similar to the FAD model. The Lopez de Bertodano model is shown to be mathematically equivalent by Burns et al. Hence, the other two models should display the same accuracy, the only difference being the model constant which its effects were assessed in the previous work [12]. The authors of the FAD model stopped short of providing guidelines on their model's applicability to which it could not be immediately determined if the FAD model is suited for the current study. Moreover, they had concluded that their model is a more general one and that it possesses 'a wide degree of universality'. Nevertheless, in one of their validation cases, the FAD model was applied to a liquid-solid flow with solid volume fractions up to 0.15 in some areas of interest and particle diameters of about $600\mu m$. With that, this work is currently putting forth the application of the FAD model to a gas-solid flow to look into how well it lends itself towards such a scenario.

The momentum exchange between phases or, interphase momentum exchange term, $\vec{R}$ obeys a constrain as shown in equation 15 and is modelled using the differences in velocities between the two phases. The mechanism dominant within this term is the drag force. The gas-solid exchange coefficient K_{sg} used here is the suggestion of Gidaspow [24] and is shown in equations 17 to 20. It is a combination of two models at different volume fractions. The Ergun [25] model at solid volume fractions larger than or equal to 0.2 and the Wen and Yu [26] model at solid volume fractions lower than 0.2. Ergun's model was experimentally determined from the pressure drop of fixed liquid-solid beds at packed conditions while Wen and Yu's model was correlated from the experiments of particle settling over wide ranges of

8

volume fractions. The bulk viscosity λ_s is obtained from the total stress tensor by Lun et al. [13] with an additional term on the right hand side of equation 21 that accounts for the particles' inelasticity.

The solids pressure (equation 7), which arose from the normal components of the stress, contained both a kinetic and collisional part. Similarly, for the shear stress, these two components should be present. The solids shear viscosity μ_s is written as consisting of two parts, collisional and kinetic part. The collisional part (equation 23) is obtained by Lun et al. [13] which is the same expression as obtained by the work of Gidaspow [24]. The kinetic part is originally obtained by Lun et al. [18]. However, Gidaspow [24] argued that a correctional factor of $1/[\eta(2 - \eta)]$ in Lun's expression is insignificant for a coefficient of restitution of 0.9, with less than a 0.3% difference. Hence, the kinetic part is as shown in equation 24.

The standard k-ϵ turbulence model is used for the gas phase turbulence and standard wall functions are used. For the Eulerian granular model, a 'per-phase' turbulence modelling was applied, where a set of separate k-ϵ turbulence equations was solved for each phase. Equations 25 and 26 show the standard $k - \epsilon$ turbulence model applied to the solid phase where the interphase turbulence interaction is included.

2.3 Meshing and convergence

A blocking strategy is applied to the full-scale industrial pipeline to obtain an unstructured hexahedral mesh. Due to the large domain size, it is fairly computationally expensive even during the mesh generation stage. In this study the cells are now sized at about $0.004 \times 0.004 \times 0.008 m$. Earlier, a mesh dependency test [12] was conducted on three different sized meshes with the same numerical model. It was found that two of the finer meshes did not

differ while the coarser mesh only differs a little from the other two. Based on this, the coarser mesh is applied in this study due to its massive computational resource advantage as there are much lesser cells. The number of cells that span the pipe diameter is 74 and no other treatment is applied for the bends. Inaccuracy is projected to be acceptable based on the mesh dependency test, as well as given the massive computational domain of the full-scale pipeline. Figure 3 shows the hexahedral mesh generated. The mesh requires about 400 CPU hours for each steady-state simulation. Together with the applied time-step size, the mesh requires about 1,500 CPU hours for each second of transient flow time simulated. The transient test case is simulated for 35 seconds and requires over 50,000 CPU hours.

2.4   Problem description

To begin with, the first set of simulations is performed under steady-state conditions to study the conveying process at a macro level. The pressure and flowrates of each phase (i.e. air and cement flows) are compared against the bulk flow data to ensure that the model is able to simulate the flow problem to a reasonable degree of accuracy. The inlet is a pressure inlet set at the air mover back pressure of 1.8*bars* and the outlet is a pressure outlet for atmospheric pressure (i.e. 0*Pa* gauge). Material properties of ordinary Portland cement are obtained from [27]. The material density is defined as 3,200*kg/m^3* and the particle diameter as 21*μm*. At the walls, different treatments are applied for both of the phases. A no-slip condition is applied for the gas phase and a specularity coefficient of 0.6 is applied for the solid phase, similar to an earlier study by the authors [12] where it produced good agreements with real-world observations. The specularity coefficient is used for a rough wall and it defines the collision characteristics of a particle with the wall, with a value of 0 being a perfectly smooth wall. Next, the conveying characteristics of the pneumatic conveying system under different conveying conditions are investigated. Conveying pressure is reduced in steps from 1.8*bars*

10

to 1.5*bars* to look into the impact on cement conveying in situations where the air pressure provided by the unloading system may not be as high. Also, JPPL is not be able to increase conveying pressures beyond 1.8*bars* as the air movers are located on the ships themselves. For each different conveying pressure, the inlet solids volume fraction is also varied (0.05, 0.10, 0.15 and 0.20). This will vary the solids loading ratio (SLR) to about 21.4, 45.1, 71.7 and 101.5 respectively. SLR is the ratio, by mass, of the cement to the air at the inlet. The value of SLR remains fairly constant along the pipeline and is, therefore, a measure favoured by the industry partner. All other parameters remain constant. For the steady-state simulations, an arbitrary solids volume fraction of 0.1 is applied to the whole domain as an additional initial condition which would improve convergence behaviour.

Lastly, a transient simulation is performed to gain insight into the cement flow characteristics within the pipe. The flow conditions are identical to the first steady-state case. The time step size was set to $1 \times 10^{-4}s$. The time step size is selected based on the condition that $v\Delta t < \Delta x$. The fully-developed numerical solution from a single-phase gas flow is applied to the domain as an initial condition prior to all the simulations. However, the solids are introduced at the inlet as a uniform distribution. This was done as a numerical means to save computational time and improve convergence behaviour.

3   Results and discussion

3.1   Steady-state simulations

3.1.1   Effects of pipeline inlet pressure

Figure 4 plots the pressure against the pipe physical distance, where total pressure values along the various location of the pipe axis are extracted from the steady-state simulation solutions. This set of data is obtained from four different inlet pressures with all the same

11

inlet cement volume fraction of 0.1. This equates to an SLR of about 45.12. The four lines represent different pressures applied at the inlet boundary condition, from 1.5 to 1.8*bars*. The inlet of the pipe is labelled 0*m* and the outlet is 156.2*m*, with the grey columns indicating the 90° bend locations. The bends are numbered one to five for easy reference. Results show that there is a distinctly higher pressure drop along each of the pipe bend as compared to straight pipe sections and that the orientation of the pipe bend also affects the extent of the pressure drop. In the current setup, only bend three consists of a horizontal-to-horizontal (HH) bend and the pressure drop along this pipe bend is lesser. The other four pipe bends are either a horizontal-to-vertical (HV) or vertical-to-horizontal (VH) bend. This behaviour is qualitatively similar to the conclusion drawn previously by Ibrahim et al. [4] where they had performed a numerical study on single bends for gas-particle flows in different bend orientation using the Lagrangian approach. They had concluded that pressure drop is greatly affected by the orientation of the bend. However, the current simulations also further revealed that there is practically no difference between HV and VH pipe bends with regards to the pressure drop. Table 1 presents the pipe bend pressure drop data in numerical form. In the last column, the pressure drop of bend 2 is divided by the square of the local mean velocity of the flow. The results suggest that pressure drop is a function of the velocity squared, where the mean velocity is obtained through the software post-processor's surface integral function. The pressure drop is also more pronounced when it is a vertical pipe section (between bends one and two, and between bends four and five) due to the additional driving force needed to overcome gravitational effects acting on the material being conveyed.

Table 1 Numerical details of pressure drop per unit length along pipe bends

Conveying pressure	Bend 1 (HV)	Bend 2 (VH)	Bend 3 (HH)	Bend 4 (HV)	Bend 5 (VH)	$\dfrac{\Delta p}{v^2}$
1.8 *bars*	2948 *Pa*	2930 *Pa*	2051 *Pa*	2968 *Pa*	2846 *Pa*	6.67
1.7 *bars*	2842 *Pa*	2804 *Pa*	1951 *Pa*	2858 *Pa*	2804 *Pa*	6.60
1.6 *bars*	2729 *Pa*	2681 *Pa*	1849 *Pa*	2751 *Pa*	2663 *Pa*	6.59
1.5 *bars*	2648 *Pa*	2594 *Pa*	1718 *Pa*	2640 *Pa*	2600 *Pa*	6.60

Theoretically, the magnitude of the pressure drop across the bends can be calculated. Chambers and Marcus [28] presented empirical formulations to calculate pressure drops along a horizontal pipe, vertical pipe or pipe bends, although the basis for its derivation was not presented. Even so, other researchers [29-31] had used the model to success. Later models, such as that proposed by Pan [10] and Pan and Wypych [32], provided derivations and experiments were used to determine the exponents in their formulation. Table 2 shows the models used to calculate the pressure drop across various pipe sections and the respective definitions of newly introduced terms are included in the same table.

Figure 5 shows the comparison between pressure drop calculated from the empirical formulations against the present numerical simulation results. The pipe bend data is from bend 2 and the vertical and horizontal pipe section from the upstream and downstream section of bend 2 respectively. Both empirical calculations and numerical simulation results match up closely, with the pipe bend and vertical pipe section pressure drops to be within 5% discrepancies. One possible reason with the horizontal pipe section having a larger but nevertheless reasonable <10% discrepancy is that the empirical formulation is dependent on the pipe roughness, and pipe roughness effects are likely to be more considerable in horizontal pipe sections. In the present case, the pipe roughness is accounted for by the specularity coefficient used in the numerical simulations that determine the shear forces

13

Table 2 Empirical relations used for calculation of the pressure drop across various pipe sections

Horizontal pipe	$\Delta p = \left(\lambda_g + SLR \times \lambda_s\right)\dfrac{\rho_g v_g^{\,2}}{2d} l_h$
	$\lambda_g = 1.325\left[\ln\left\{\dfrac{\epsilon_p}{3.7d} + \dfrac{5.74}{Re^{0.9}}\right\}\right]^{-2}$
	$\lambda_s = 2.1 Fr_s^{\,0.25}\left(\dfrac{d}{d_s}\right)^{0.1}\dfrac{1}{SLR^{0.3} Fr}$
Vertical pipe	$\Delta p = SLR \times \rho_g g l_v \dfrac{v_g}{v_s}$
Bends	$\Delta p = B(1 + SLR)\rho_g \dfrac{v_g^{\,2}}{2}$, $B = 0.5$
	where l_h and l_v are the length of the respective pipe,
	ϵ_p is the absolute pipe roughness,
	Froude number $Fr = \dfrac{v_g^{\,2}}{gd}$,
	particle Froude number $Fr_s = \dfrac{4gd_s(\rho s - \rho_g)/(3C_d\rho_g)}{gd_s}$,
	$C_d = \dfrac{24}{Re_p}\left(1 + \dfrac{3Re_p}{16}\right)$ and
	$Re_p = \dfrac{v_s \rho_g d_s}{\mu_g}$

associated with the solid phase at the wall. For a wall roughness height that is comparable to the particle diameter, the specularity coefficient will be large [33]. However, this value is not easily determined with an explicit expression but has to be compared against experiments [34]. However, a value of 0.6 that had been used in accordance with an earlier study by the authors as mentioned previously, which had been observed to work satisfactory. Nevertheless, the specularity coefficient has no effect on the gas phase and can be regarded as a smooth wall when the gas phase is concerned. Hence, it is seen that the pressure drop is lesser within the simulation results.

3.1.2 Equivalent length for pipe bends

It will be useful for industrial applications if the pressure drops across the 90° pipe bends can be related to the pressure drop across a straight pipe section. For single-phase fluid flows, this has been well-established as the "equivalent pipe length" concept. However, this is not the case for gas-particle flows such as the ones encountered here. This value of pressure drop per unit length is convenient for designers to gain a sense of the type of conveying mechanism (i.e. dense or dilute flow) the pipeline is operating in [35]. It is also an important parameter to consider when designing pneumatic conveying pipelines [36, 37]. Figure 6 represents the ratio of pressure drop per metre of pipe bend against pressure drop per metre of straight pipe. It compares the pressure drop across bend 2 with pressure drop across the long straight horizontal pipe section further downstream of bend 2. This ratio is observed to be a little higher than three for conveying pressure of 1.5 *bars*. This means that for every metre of pipe bend (measured along the pipe axis), it is equivalent to three metres of straight pipe in terms of pressure drop. The equivalent pipe length is seen to be dependent on the conveying pressure which is inadvertently caused by increased conveying velocities at higher conveying pressures.

With the current dataset, it reveals that the ratio varies linearly with the inlet conveying pressure, thereby allowing for the possibility of extrapolating pressure losses across pipe bends for different conveying pressures. However, note that the extent to which this linear relationship holds beyond the current conveying pressures is not investigated. The ratio is also expected to be dependent on the material being conveyed. Nevertheless, the equivalent length results obtained from the current simulations is similar to results obtained from experiments conducted by Spedding and Benard [38] for gas-liquid flows, where their results also show a monotonically increasing ratio. However, it should be noted that the current

15

conclusion of the pressure drop ratio being a little over 3 is only determined for the present pipeline and flow scenarios and the exact pressure drop ratio will vary depending on the actual situation. Nevertheless, the current pipe geometry is that of an actual pipeline in operation within the industry and the present results provide insights into their designs. Hence, these findings will be useful for individuals or organizations involved with full-scale pneumatic conveying pipelines, be it research or system design.

3.1.3   Conveying characteristics

The pipeline conveying characteristics are now investigated by varying the inlet material feed rate in addition to the different conveying pressures. Inlet solids volume fractions are varied from 0.05 to 0.2 and Figure 7 presents the air and cement flowrate at the outlet (left and right axis, respectively). As the maximum capacity of the dust collector at the outlet is 12,000 m^3/h, the horizontal dashed line at the left denotes this limit. With the air and cement flowrate plotted on the same graph, it is possible to ascertain if the dust collector can handle the conveying operation at a certain conveying pressure and SLR. Also, it is possible to read off the maximum conveying capacity (*tph*) of the pipeline. For example, with each outlet air flowrate and SLR, one can then move up or down to the cement outlet flowrate at the corresponding conveying pressure and estimate the cement conveying rate on the right axis. Apart from applying this data directly to operational situations, the data here provides a glimpse of the conveying characteristics that might be typical of a system like this. It is seen that at all conveying pressures, the amount of air used decreases with increasing SLR (blue graphs). One immediate observation is that the relationship is not linear. Also, the amount of cement conveyed increases with increasing SLR (red graphs) and this relationship is also observed to be non-linear (though less pronounced than the air flow rate). Therefore, it will not be the most efficient way to simply increase the inlet SLR, where the power requirements

16

for the conveying system can increase significantly. This will also be physically limited by the cement properties, such as the maximum packing limit or the saltation velocity. The maximum packing limit is how much cement that can actually fit into the pipe cross-section. The saltation velocity is the minimum velocity of the conveying medium that is required to pick up the cement. Any velocities lower than the saltation velocity will result in the cement depositing at the bottom of the pipe. While this set of data is not able to predict these limits, the general trends of the conveying characteristics can be inferred.

In all, the results of the steady-state simulations presented so far provide an optimistic view that the actual pneumatic conveying process is well simulated. Simulation results match with both the bulk flow data and theoretical calculations. It is also a demonstration that the FAD model is adequate in the current study and can predict conveying rates that matches data provided by the industry. Arguably, the results from steady-state simulations are extremely handy only in terms of practical design or operations. However, the primary importance highlighted in this work is that the steady-state simulations here manage to bridge the gap between theoretical research and industrial applications. It is believed that with decreasing computational cost and increasing robustness in numerical simulations, such a method of directly investigating an industrial scale system will become increasingly feasible.

3.2   Unsteady state simulations

3.2.1   Particle rope

Results of unsteady-state simulations presented here will illustrate the intricate details of the solids flow behaviour within the pipe. The transient simulation results that were averaged over the last 10 seconds of the simulated flow time produce reasonable agreements with the steady state results. For example, the pressure drop per metre across the vertical pipe section

17

(as compared to steady state simulation) is 2119Pa (1919Pa), across the bend is 2790Pa (2923Pa) and across horizontal pipe section is 963Pa (866Pa). Also, the cement flow throughput is 471tph (461tph).

Figure 8 shows the iso-surface plot of 0.2 cement volume fraction at pipe bend number two which is a VH bend. Cross-sectional views of volume fraction plots are also included in the figure. The iso-surface plot can be approximated to be the particle rope within the pipe. The particle rope, which is a concentration of particles at certain regions of the pipe, is seen to navigate the pipe bend adhering to the outer part of the pipe bend. This is expected due to inertial forces of the cement particles. When exiting the pipe bend, the particle rope is seen to follow one side of the pipe wall (farther side, in this case) to the bottom of the pipe. This is in contrast to other studies which saw the particle rope settle down in the middle, through the axis of the pipe. The difference here is due to the pipe geometry prior to the bend. For the current geometry, note that an HV pipe bend precedes the VH pipe bend. Such an arrangement of pipe bends changes the position of the particle rope entering the pipe bend and also alters the secondary flows within the pipe (see Section 3.2.2). Figure 9(a) illustrates the bend positions in which the plots from later figures are extracted from, while Fig. 9(b) illustrates how the position of the particle rope within the bend will be quantified later. For a better understanding, Figure 10-12 shows the cross-sectional contour plots of cement volume fraction.

Figure 10 shows the various plots for the vertical pipe section, where cross-sections of a distinct particle rope on the right side of the pipe can be observed. This particle rope is formed by the first bend. With the very short downstream section of the first bend, the particle rope does not disperse and enters the second bend with the structure of the particle

18

rope being more or less preserved. In Figure 11, after the particle rope enters the bend, inertial forces and secondary flows start to alter its position. After 30°, the particle rope is seen to start dispersing due to secondary flow structures. At the same time, the particles also begin to move towards the pipe wall and shift their locations from the right side of the pipe towards the outer bend due to inertial forces.

After the bend (Figure 12) the concentration of particles did not make a complete revolution over to the left side of the pipe before falling down to the bottom of the pipe. Instead, it traces its path back on the right side of the pipe before falling to the bottom of the pipe in contrast to the findings of [5] where the particles spiral around the pipe walls. This is largely due to the structure of the secondary flows which will be cover in more detail later. By observing the sequence of cross-sectional plots downstream of the bend, the particles are seen to slosh around the bottom of the pipe before the sloshing damps down and the particles traverse to the bottom of the pipe. This sloshing motion is not apparent when presented in the three-dimensional view (Figure 8). By simple measurements, the location of higher particle concentrations can be represented in a graphical format. The area of highest particle concentration is determined by the thickest location of the 0.2 volume fraction contour, as measured from the pipe wall. By assigning the top of the pipe as 0°, the solid line plot in Figure 13 shows the location of the rope. An illistration is shown previously on Figure 9(b). The grey region refers to the region of pipe bend and the region to the right of the grey box being the horizontal pipe section up to 100 pipe diameters (d) downstream.

The particle rope is seen to enter the pipe bend at an angle of about 90° formed due to the upstream HV pipe bend. Within the pipe bend, it shifts its position towards 0°, being the outside of the pipe bend. Then, after exiting the pipe bend, it falls rapidly to the bottom of the

pipe and displays an oscillatory motion. This motion is the sloshing of the particles at the bottom of the pipe, seemingly highly reliant on gravitational effects. It is interesting to note that the angular position of higher concentration of particles can be fitted with an under-damped graph (dashed line in Figure 13) starting at 0 d after the bend. The equation of this under-damped curve is provided in the figure. By applying theories from damped harmonic oscillations, system characteristics such as the angular frequency and damping ratio can be obtained. At this point, these characteristics are postulated to be linked to the viscous forces of the material conveyed and is a topic where future work can be done in greater detail.

3.2.2 Secondary flows

Secondary flow structures of a fluid inside a simple pipe bend are well documented in the literature. As inertial forces take over when navigating a pipe bend, the fluid tends to move towards the outside of the pipe bend. It normally forms a symmetrical pair of counter-rotating vortices and sometimes two pairs of counter-rotating vortices in 180° bends [39]. A snapshot of secondary flow structure in the current flow case is shown in Figure 14. It is a velocity vector plot of velocities tangential to the displayed plane. While the general behaviour of fluid moving out towards the outside of the pipe bend is still present, the secondary flow structure is no longer symmetric. Also, there exists a weaker pair of counter-rotating vortices alongside a dominating pair. The secondary flow structures are indisputably different in both cases.

In Figure 15, where the secondary flow structures in the upstream section are shown, the symmetrical pair of counter-rotating vortices formed by the previous pipe bend is seen to slowly dissipate until it reaches the entrance of the next pipe bend. They are, however, not fully dissipated and the velocity profile of the fluid does not approach that of a uniform

20

turbulent flow profile. Hence, after it enters the pipe bend, the residual secondary flow from the previous pipe bend interferes with the flow producing non-symmetrical secondary flows. Figure 16, which shows the secondary flows within the VH pipe bend, reveals a pair of weaker counter-rotating vortices that is only vaguely present from 30° onwards. They are then seen to strengthen and take shape where it is distinctly visible at the 60° location. Thereafter, it merges with the stronger pair to produce a disorganized secondary flow pattern.

On the other hand, Figure 17(a) shows the secondary flow structure downstream of the pipe bend. After exiting the pipe bend, the secondary flow vortices start to merge into a single clockwise vortex. It is evident that this clockwise secondary flow is one of the reasons as to why the particle rope does not complete a revolution around the wall of the pipe (see Figure 8 and 12(a)). Also, by comparing the secondary flow structures with the volume fraction contour plots, particularly for $10\,d - 30\,d$, the left-to-right sloshing of the material conveyed in the horizontal pipe section is accompanied by a change in the direction of the secondary flow vortex. In addition to that, it can be seen from $20\,d - 30\,d$ that the change in sloshing direction in the volume fraction contour plot actually lags the direction change of secondary flow in the tangential velocity vector plot. This suggests that, apart from gravitational forces, secondary flow patterns also play a part in determining the flow behaviour of the conveyed material. Beyond $50\,d$, secondary flow patterns are almost non-existent and the sloshing behaviour is entirely dominated by gravitational forces.

It should be highlighted that the transient flow results presented herein only represents a small subset of the data obtained from the numerical simulations. While additional data are available, including them will render the current paper too long and less readable. Nevertheless, the current data from one of the bend that is presented here expands on the

21

limited knowledge associated with a combination of pipe bends. Apart from the work of Schallert and Levy [5], literature detailing detailed flow behaviour when more than one pipe bend is used remains limited. Hence, the present findings broaden the current understanding of cement flows within a pipeline with several different pipe bends which is a situation that is commonly found in industry implementations of pneumatic conveying.

3.2.3 Comparisons between different bends

Figure 18 shows the volume fraction plot at the 0°, 45° and 90° marks of bend 1 where the outside wall of the bend is at the top. The particles enter the bend as a rather uniform distribution and inertial effects causes a particle rope to form on the outside wall. This mechanism is well documented in literature. On the other hand, Fig.19 shows the four other bends, numbers 2 to 5, being a VH, HH, HV and VH bend respectively. The outside of the bend is on the top and the plots are also taken at the 0°, 45° and 90° marks. Immediately, it can be observed that the positions of the particle rope are different in each case and is greatly dependent on the orientation of the pipe bend. Less apparent is its dependence on the upstream conditions of the bend. For example, bends 2 and 5 are both VH bends which are preceded by HV bends of the same orientation. However, there is significantly less roping in bend 5 as compared to bend 2. This is due to the length of the pipe connecting the two bends in which a longer connecting length for bend 5 facilitated the dispersion of the particle rope. Furthermore, it is affected by the outlet shortly downstream of the bend. The entry to bend 3 shows a relatively settled layer of particles along the bottom of the pipe due to the extended length of the horizontal pipe upstream of the bend. Upon entering the bend, they slosh towards the outside of the bend and collapse back to the bottom of the pipe. In bend 4, the particle rope does not show much transformation throughout the bend because the rope enters the bend on the outside wall of the bend. Thus, the particle rope follows through the bend

22

along the outside wall. Therefore, it is seen that the pathway of the particle rope strongly depends on both the orientation and conditions upstream of the bend.

4   Conclusions

An Eulerian granular model is applied to an industrial scale pneumatic conveying pipe to study the flow characteristics of the material being conveyed. Steady-state numerical results are observed to agree well with bulk flow data that are obtained from JPPL, indicating an appropriate application of the numerical model. Subsequently, the conveying pressures and inlet loading are varied to observe the relationships between the parameters and conveying output capacity. The relationship between output and both inlet pressure and loading is found to be non-linear, due to the physical limitations of the conveying system. Such findings will be useful to assess the impact of these parameters upon the operational capabilities of the pneumatic conveying pipe. In particular, these results also demonstrate that numerical simulations of a full-scale, operational pneumatic conveying pipe are feasible and sufficiently accurate for practical purposes.

Transient simulations are then performed on a selected flow configuration where a combination of different pipe bends is present, similar to an operational pneumatic conveying pipe. The flow behaviour in a VH bend, preceded by an HV bend, was evaluated in terms of the particle rope and flow structures. Results show that, instead of passing through the centre axis of the pipeline, the particle rope stays on the sides of the pipe wall after exiting the bend. This is due to the influences exerted by the secondary flow structures produced by the upstream bend. Also, an interesting sloshing behaviour of the conveyed material is observed and the angular position of the concentrated particles mimic that of an under-damped system. Collating with the various transient results, the preceding flow observations are partly due to

23

the secondary flow structures, on top of gravitational effects. Lastly, further investigations on the selection of the specularity coefficient in the numerical model and the viscous effects on the sloshing dynamics of the particle rope after the bend are recommended.

References

[1]   D. Mills, *Pneumatic conveying design guide*. Butterworth-Heinemann, 2003.

[2]   D. McGlinchey, A. Cowell, and R. Crowe, "CFD investigation of dense phase pneumatic conveying at a pipeline enlargement," *Particuology,* vol. 10, no. 2, pp. 176-183, 2012.

[3]   N. Behera, V. K. Agarwal, M. G. Jones, and K. C. Williams, "CFD modeling and analysis of dense phase pneumatic conveying of fine particles including particle size distribution," *Powder Technology,* vol. 244, pp. 30-37, 2013.

[4]   K. Ibrahim, M. El-Kadi, M. Hamed, and S. M. El-Behery, "Effect of bend orientation and flow direction on the behaviour of gas–solid flow," in *Proceedings 8th International Conference of Fluid Dynamics and Propulsion*, 2006, vol. 136, pp. 14-17.

[5]   R. Schallert and E. Levy, "Effect of a combination of two elbows on particle roping in pneumatic conveying," *Powder Technology,* vol. 107, no. 3, pp. 226-233, 2000.

[6]   D. McGlinchey, A. Cowell, E. Knight, J. Pugh, A. Mason, and B. Foster, "Bend pressure drop predictions using the Euler-Euler model in dense phase pneumatic conveying," *Particulate Science and Technology,* vol. 25, no. 6, pp. 495-506, 2007.

[7]   J. Li *et al.*, "Solids deposition in low-velocity slug flow pneumatic conveying," *Chemical Engineering and Processing: Process Intensification,* vol. 44, no. 2, pp. 167-173, 2005.

[8]   A. B. Makwana, A. Patankar, and M. Bose, "Effect of Dune Formation on Pressure Drop in Horizontal Pneumatic Conveying System," *Particulate Science and Technology,* vol. 33, no. 1, pp. 59-66, 2015.

[9]   S. S. Mallick and P. Wypych, "Evaluation of scaleup procedures using "system" approach for pneumatic conveying of powders," *Particulate Science and Technology,* vol. 28, no. 1, pp. 41-50, 2010.

[10]   R. Pan, "Improving scale-up procedures for the design of pneumatic conveying systems," Department of Mechanical Engineering, University of Wollongong, New South Wales, Australia, 1992.

[11]   S. S. Mallick and P. W. Wypych, "On improving scale-up procedures for dense-phase pneumatic conveying of powders," *Particulate Science and Technology,* vol. 29, no. 5, pp. 407-427, 2011.

[12]   J. Heng, T. H. New, and P. A. Wilson, "On the application of an Eulerian granular model towards dilute phase pneumatic conveying," *Powder Technology,* vol. 327, pp. 456-466, 2018.

[13] C. Lun, S. B. Savage, D. Jeffrey, and N. Chepurniy, "Kinetic theories for granular flow: inelastic particles in Couette flow and slightly inelastic particles in a general flowfield," *Journal of Fluid Mechanics,* vol. 140, pp. 223-256, 1984.

[14] S. Savage and D. Jeffrey, "The stress tensor in a granular flow at high shear rates," *Journal of Fluid Mechanics,* vol. 110, pp. 255-272, 1981.

[15] M. Ehsani, S. Movahedirad, S. Shahhosseini, and M. Ashtiani, "Effects of Restitution and Specularity Coefficients on Solid‐Liquid Fluidized Bed Hydrodynamics," *Chemical Engineering & Technology,* vol. 38, no. 10, pp. 1827-1836, 2015.

[16] J. Ding and D. Gidaspow, "A bubbling fluidization model using kinetic theory of granular flow," *American Institute of Chemical Engineers Journal,* vol. 36, no. 4, pp. 523-538, 1990.

[17] M. Syamlal, W. Rogers, and T. J. O'Brien, "MFIX documentation: Theory guide," *National Energy Technology Laboratory, Department of Energy, Technical Note,* 1993.

[18] D. Gidaspow, R. Bezburuah, and J. Ding, "Hydrodynamics of circulating fluidized beds: kinetic theory approach," Illinois Institute of Technology, Chicago, IL (United States). Department of Chemical Engineering1991.

[19] S. Ogawa, A. Umemura, and N. Oshima, "On the equations of fully fluidized granular materials," *Journal of Applied Mathematics and Physics (ZAMP),* vol. 31, no. 4, pp. 483-493, 1980.

[20] R. Brown and P. Hawksley, "Packing of regular (spherical) and irregular particles," *Nature,* vol. 156, no. 3962, pp. 421-422, 1945.

26

[21] A. D. Burns, T. Frank, I. Hamill, and J. Shi, "The Favre averaged drag model for turbulent dispersion in Eulerian multi-phase flows," in *5th International Conference on Multiphase Flow*, 2004, vol. 4, pp. 1-17.

[22] O. Simonin and P. Viollet, "Modelling of turbulent two-phase jets loaded with discrete particles," *FG Hewitt, et al., Phenomena in multiphase yow,* vol. 259, 1990.

[23] d. B. M. Lopez, "Turbulent bubbly two-phase flow in a triangular duct," 1993.

[24] D. Gidaspow, *Multiphase flow and fluidization: continuum and kinetic theory descriptions*. Academic Press, 1994.

[25] S. Ergun, "Fluid flow through packed columns," *Chemical Engineering Progress,* vol. 48, pp. 89-94, 1952.

[26] C. Wen and Y. Yu, "Mechanics of fluidization," in *Chemical Engineering Progress Symposium Series*, 1966, vol. 6, pp. 100-101.

[27] H. F. Taylor, *Cement chemistry*. Thomas Telford, 1997.

[28] A. Chambers and R. Marcus, "Pneumatic conveying calculations," in *Second International Conference on Bulk Materials Storage, Handling and Transportation: 1986; Preprints of Papers*, 1986, pp. 49-52: Institution of Engineers, Australia.

[29] S. S. Mallick, "Modelling of fluidised dense-phase pneumatic conveying of powders," Ph.D. Dissertation, Centre for Bulk Solids and Particulate Technologies, Faculty of Engineering, University of Wollongong, New South Wales, Australia, 2009.

[30] M. Jones and K. Williams, "Solids friction factors for fluidized dense-phase conveying," *Particulate Science and Technology,* vol. 21, no. 1, pp. 45-56, 2003.

[31] G. Setia, S. S. Mallick, R. Pan, and P. W. Wypych, "Modeling solids friction factor for fluidized dense-phase pneumatic transport of powders using two layer flow theory," *Powder Technology,* vol. 294, pp. 80-92, 2016.

[32] R. Pan and P. Wypych, "Dilute and dense phase pneumatic conveying of fly ash," in *Proceedings of the 6th International Conference on Bulk Materials Storage and Transportation, Wollongong, NSW, Australia*, 1998, pp. 183-189.

[33] T. Li and S. Benyahia, "Revisiting Johnson and Jackson boundary conditions for granular flows," *American Institute of Chemical Engineers Journal,* vol. 58, no. 7, pp. 2058-2068, 2012.

[34] C. Loha, H. Chattopadhyay, and P. K. Chatterjee, "Euler-Euler CFD modeling of fluidized bed: Influence of specularity coefficient on hydrodynamic behavior," *Particuology,* vol. 11, no. 6, pp. 673-680, 2013.

[35] F. A. Zenz, "Two-phase fluid-solid flow," *Industrial & Engineering Chemistry,* vol. 41, no. 12, pp. 2801-2806, 1949.

[36] M. Bradley, "Pressure losses caused by bends in pneumatic conveying pipelines, effects of bend geometry and fittings," *Powder Handling and Processing,* vol. 2, no. 2, pp. 315-321, 1990.

[37] Y. Morikawa, Y. Tsuji, K. Matsui, and Y. Jittani, "Pressure drops due to pipe bends in air-solids two phase flows; circular and elliptical bends," *International Journal of Multiphase Flow,* vol. 4, no. 5, pp. 575-583, 1978.

[38] P. Spedding and E. Benard, "Gas–liquid two phase flow through a vertical 90 elbow bend," *Experimental Thermal and Fluid Science,* vol. 31, no. 7, pp. 761-769, 2007.

[39]   M. Rowe, "Measurements and computations of flow in pipe bends," *Journal of Fluid Mechanics,* vol. 43, no. 04, pp. 771-783, 1970.

Appendix

Equations of the Eulerian granular model

The mass conservation equation of the gas phase is:

$$\frac{\partial}{\partial t}(\alpha_g \rho_g) + \nabla \cdot (\alpha_g \rho_g \overrightarrow{v_g}) = 0 \tag{1}$$

and the momentum conservation of the gas phase is:

$$\frac{\partial}{\partial t}(\alpha_g \rho_g \overrightarrow{v_g}) + \nabla \cdot (\alpha_g \rho_g \overrightarrow{v_g}\overrightarrow{v_g}) = -\alpha_g \nabla p + \nabla \cdot \overline{\overline{\tau_g}} + \alpha_g \rho_g \vec{g} \tag{2}$$

where $\overline{\overline{\tau}}_g$ is:

$$\overline{\overline{\tau_g}} = \alpha_g \mu_g \left(\nabla \overrightarrow{v_g} + \nabla \overrightarrow{v_g}^T \right) + \alpha_g \left(-\frac{2}{3}\mu_g \right) \nabla \cdot \overrightarrow{v_g}\overline{I} \tag{3}$$

The mass conservation equation of the solid phase is:

$$\frac{\partial}{\partial t}(\alpha_s \rho_s) + \nabla \cdot (\alpha_s \rho_s \overrightarrow{v_s}) = 0 \tag{4}$$

and the momentum conservation of the solid phase is:

$$\frac{\partial}{\partial t}(\alpha_s \rho_s \overrightarrow{v_g}) + \nabla \cdot (\alpha_s \rho_s \overrightarrow{v_s}\overrightarrow{v_s}) = -\alpha_s \nabla p + \nabla \cdot \overline{\overline{\tau}}_s + \alpha_s \rho_s \vec{g} + \overrightarrow{F_{td,s}} + \overrightarrow{R_{gs}} \tag{5}$$

where $\overline{\overline{\tau}}_s$ is:

$$\overline{\overline{\tau_s}} = \alpha_s \mu_s \left(\nabla \overrightarrow{v_s} + \nabla \overrightarrow{v_s}^T \right) + \alpha_s \left(\lambda_s - \frac{2}{3}\mu_s \right) \nabla \cdot \overrightarrow{v_s}\overline{I} \tag{6}$$

The pressure tensor p_s is:

$$p_s = \alpha_s \rho_s \Theta_s + 2\rho_s(1 + e_{ss})\alpha_s^2 g_{0,ss}\Theta_s \tag{7}$$

where Θ_s is granular temperature, e_{ss} is coefficient of restitution for collision and $g_{0,ss}$ is

the radial distribution function.

The granular temperature is proportional to the particles' fluctuation:

$$\Theta_s = \frac{1}{3}\overline{u_{\iota,s}u_{\iota,s}} \tag{8}$$

and the transport equation for granular temperature is:

$$\frac{3}{2}\left[\frac{\partial}{\partial t}(\rho_s\alpha_s\Theta_s) + \nabla \cdot (\rho_s\alpha_s\vec{v}_s\Theta_s)\right] = \left(-p_s\bar{\bar{I}} + \bar{\bar{\tau}}_s\right):\nabla\vec{v}_s + \nabla \cdot \left(k_{\Theta_s}\nabla\Theta_s\right) - \gamma_{\Theta_s} + \phi_{gs} \tag{9}$$

where the diffusion coefficient $k_{\Theta s}$ is:

$$k_{\Theta_s} = \frac{15d_s\rho_s\alpha_s\sqrt{\Theta_s\pi}}{4(41 - 33\eta)}\left[1 + \frac{12}{5}\eta(4\eta - 3)\alpha_s g_{0,ss} + \frac{16}{15\pi}(41 - 33\eta)\eta\alpha_s g_{0,ss}\right] \tag{10}$$

with $\eta=0.5(1+e_{ss})$ and the collisional dissipation of energy $\gamma_{\Theta s}$ is:

$$\gamma_{\Theta_s} = \frac{12(1 - e_{ss}^2)g_{0,ss}}{d_s\sqrt{\pi}}\rho_s\alpha_s^2\Theta_s^{\frac{3}{2}} \tag{11}$$

and $\phi_{gs}=-3K_{gs}\Theta_s$ is the energy exchange between the phases.

The radial distribution function $g_{0,ss}$ is:

$$g_{0,ss} = \left[1 - \left(\frac{\alpha_s}{\alpha_{s,max}}\right)^{\frac{1}{3}}\right]^{-1} \tag{12}$$

where $\alpha_{s,max}$ is the packing limit of the solids phase.

30

The turbulent dispersion force $\vec{F}_{td,s}$ in equation 5 is:

$$\vec{F}_{td,s} = C_{TD} K_{sg} \frac{D_s}{\sigma_{gs}} \left(\frac{\nabla \alpha_g}{\alpha_g} - \frac{\nabla \alpha_s}{\alpha_s} \right) \tag{13}$$

where C_{TD} is a modifiable constant, K_{sg} is the interphase momentum exchange coefficient, σ_{gs} is the turbulent Prandtl number and the dispersion scalar D_s is estimated by:

$$D_s = \frac{\mu_{ts}}{\rho_s} \tag{14}$$

The momentum exchange between phases or, interphase momentum exchange term, $\vec{R}$ obeys the following constrain that:

$$\overrightarrow{R_{sg}} = -\overrightarrow{R_{gs}} \tag{15}$$

and is modelled using the differences in velocities between the two phases:

$$\overrightarrow{R_{sg}} = K_{sg} \left(\overrightarrow{v_s} - \overrightarrow{v_g} \right) \tag{16}$$

where K is an interphase momentum exchange coefficient.

The gas-solid exchange coefficient K_{sg} is:

$$K_{sg} = \frac{3}{4} C_D \frac{\alpha_s \alpha_g \rho_g |\vec{v}_s - \vec{v}_g|}{d_s} \alpha_g^{-2.65} \tag{17}$$

when $\alpha_g > 0.8$. d_s is the particle diameter and the drag function C_D is:

$$C_D = \frac{24}{\alpha_g Re_s} \left[1 + 0.15 \left(\alpha_g Re_s \right)^{0.687} \right] \tag{18}$$

with Re_s being the relative Reynolds number:

31

$$Re_s = \frac{\rho_g d_s |\vec{v}_s - \vec{v}_g|}{\mu_g} \tag{19}$$

For when $\alpha_g \leq 0.8$,

$$K_{sg} = 150 \frac{\alpha_s^{\,2} \mu_g}{\alpha_g d_s^{\,2}} + 1.75 \frac{\rho_g \alpha_s |\vec{v}_s - \vec{v}_g|}{d_s} \tag{20}$$

The bulk viscosity λ_s is:

$$\lambda_s = \frac{8}{3} \alpha_s^2 \rho_s d_s g_{0,ss} \left(\frac{\Theta_s}{\pi}\right)^{\frac{1}{2}} \times \frac{1}{2}(1 + e_{ss}) \tag{21}$$

The solids shear viscosity μ_s is written as consisting of three parts, collisional, kinetic and

frictional part:

$$\mu_s = \mu_{s,col} + \mu_{s,kin} \tag{22}$$

The collisional part is:

$$\mu_{s,col} = \frac{4}{5} \alpha_s \rho_s d_s g_{0,ss}(1 + e_{ss}) \left(\frac{\Theta_s}{\pi}\right)^{\frac{1}{2}} \alpha_s \tag{23}$$

and the kinetic part is:

$$\mu_{s,kin} = \frac{5}{96} \rho_s d_s \sqrt{\Theta_s \pi} \left[\frac{1}{\eta g_{0,ss}}\right] \left[1 + \frac{8}{5} g_{0,ss} \alpha_s \eta\right]^2 \tag{24}$$

The standard k-ε turbulence model was used for the gas phase turbulence:

32

$$\frac{\partial}{\partial t}(\alpha_s \rho_s k_s) + \nabla \cdot (\alpha_s \rho_s \overrightarrow{U_s} k_s)$$

$$= \nabla \cdot \left(\alpha_s \left(\mu_s + \frac{\mu_{t,s}}{\sigma_k} \right) \nabla k_s \right) + \alpha_s G_{k,s} - \alpha_s \rho_s \epsilon_s + K_{gs}(C_{gs} k_g - C_{sg} k_s) \quad (25)$$

$$- K_{gs}(\overrightarrow{U_g} - \overrightarrow{U_s}) \cdot \frac{\mu_{t,g}}{\alpha_g \sigma_g} \nabla \alpha_g + K_{gs}(\overrightarrow{U_g} - \overrightarrow{U_s}) \cdot \frac{\mu_{t,s}}{\alpha_s \sigma_s} \nabla \alpha_s$$

$$\frac{\partial}{\partial t}(\alpha_s \rho_s \epsilon_s) + \nabla \cdot (\alpha_s \rho_s \overrightarrow{U_s} \epsilon_s)$$

$$= \nabla \cdot \left(\alpha_s \left(\mu_s + \frac{\mu_{t,s}}{\sigma_\epsilon} \right) \nabla \epsilon_s \right)$$

$$+ \frac{\epsilon_s}{k_s} \Bigg[C_{1\epsilon} \alpha_s G_{k,s} - C_{2\epsilon} \alpha_s \rho_s \epsilon_s \qquad (26)$$

$$+ C_{3\epsilon} \left(K_{gs}(C_{gs} k_g - C_{sg} k_s) - K_{gs}(\overrightarrow{U_g} - \overrightarrow{U_s}) \cdot \frac{\mu_{t,g}}{\alpha_g \sigma_g} \nabla \alpha_g \right.$$

$$\left. + K_{gs}(\overrightarrow{U_g} - \overrightarrow{U_s}) \cdot \frac{\mu_{t,s}}{\alpha_s \sigma_s} \nabla \alpha_s \right) \Bigg]$$

- An Eulerian model is applied to a full-scale industrial pneumatic conveying system.

- Steady-state simulation matches both bulk flow data and theoretical calculations.

- Direct simulations of an industrial scale system will become increasingly feasible.

- Transient sloshing behaviour of cement mimic that of an under-damped system.

- Secondary flow patterns play a part in determining flow behaviour of cement.
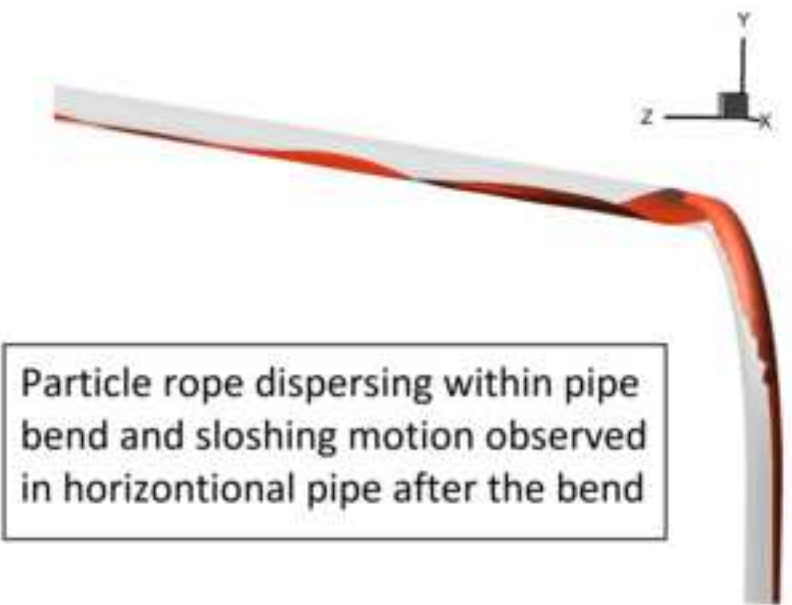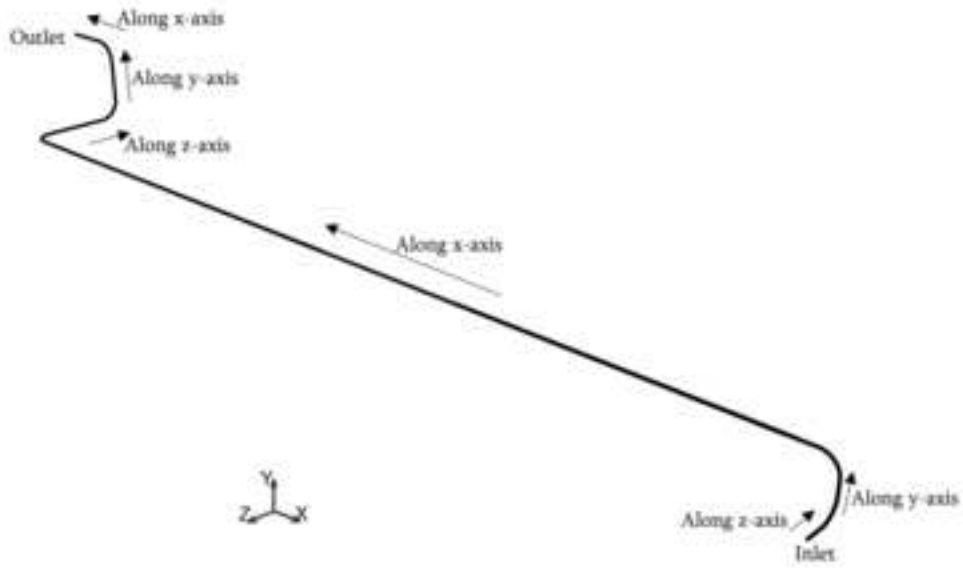
Particle rope dispersing within pipe bend and sloshing motion observed in horizontial pipe after the bend
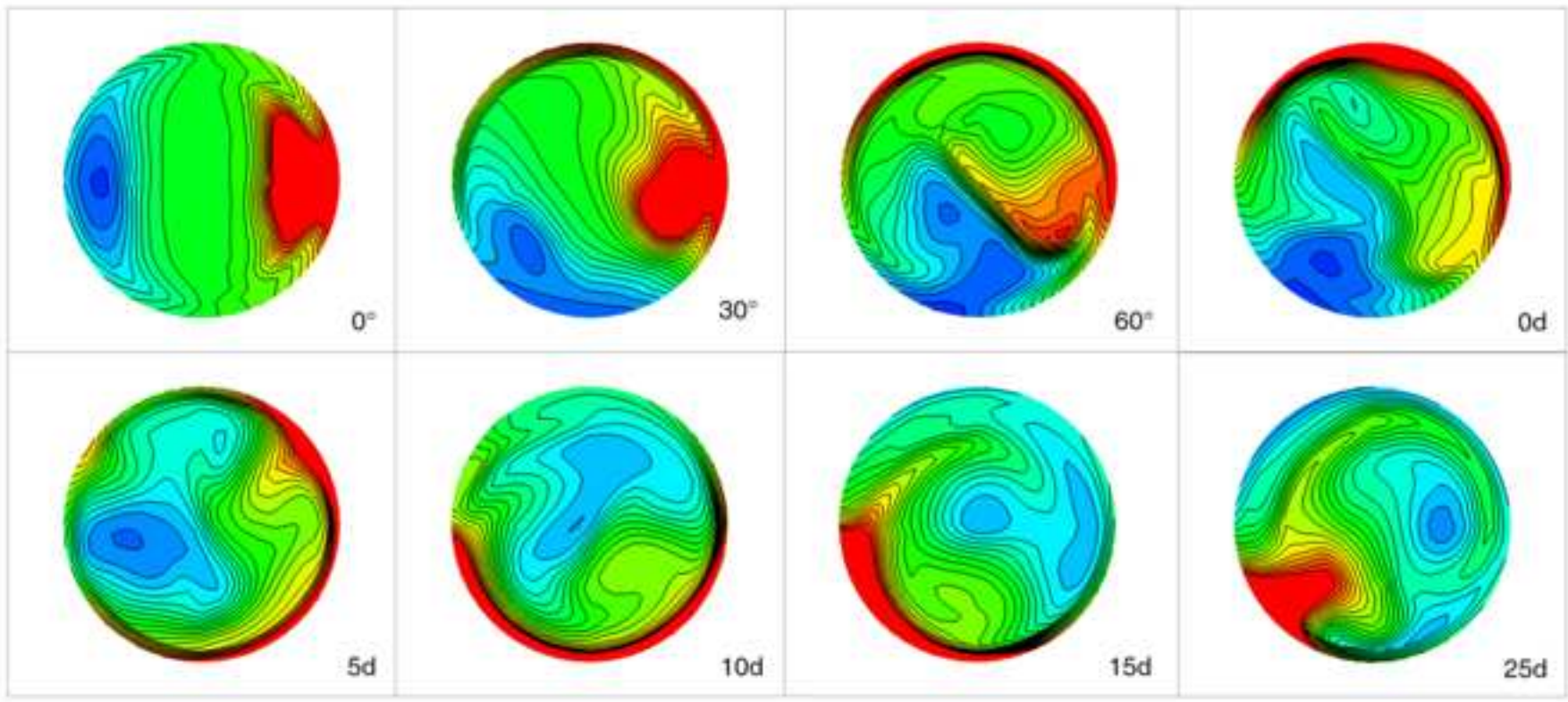
Figure captions

Figure 1   Pneumatic pipeline geometry, straight pipe sections are orthogonal to each other.

Figure 2   Pipeline dimensions (pipe diameter not drawn to scale). Also shown is the length of the straight pipe sections in terms of multiples of pipe diameter (d).

Figure 3   Hexahedral mesh generated.

Figure 4   Pressure drop along the pipeline for different conveying pressures.

Figure 5   Pressure drop comparison between calculated values and numerical simulation for bend 2, vertical pipe section upstream of bend 2 and horizontal pipe section downstream of bend 2.

Figure 6   Pressure drop ratio of bend 2 to horizontal straight pipe downstream of bend 2 for various conveying pressures simulated

Figure 7   Pipeline conveying characteristics for different solids loading ratio.

Figure 8   Iso-surface plot of 0.2 cement volume fraction at bend number two.

Figure 9   Illustration of (a) bend positions and (b) rope position.

Figure 10   Cement volume fraction plot upstream of the bend at various multiple of pipe diameter (d) leading up to the bend as indicated. Top side being the outside of the upcoming bend and -1d being nearer to the entrance of the bend.

Figure 11   Cement volume fraction plot within the bend at various locations within the bend as indicated. Top side being the outside of the bend and 0° being the entrance of the bend.

Figure 12(a)   Cement volume fraction plot downstream of the bend at 0d to 30d as indicated. Bottom side being the bottom of the pipe and 0d being the exit of the bend.

Figure 12(b)   Cement volume fraction plot downstream of the bend at 35d to 100d as indicated. Bottom side being the bottom of the pipe.
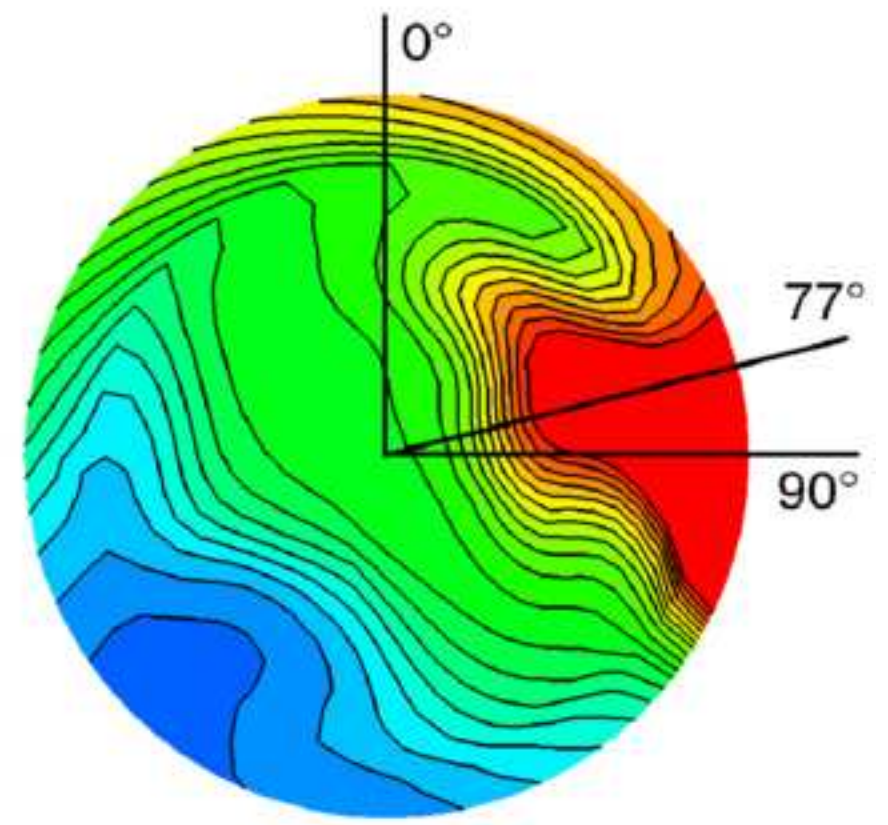
Figure 1
Click here to download high resolution image

Outlet

Along x-axis

Bend 5

Along y-axis

Along z-axis

Bend 1 - HV bend
Bend 2 - VH bend
Bend 3 - HH bend
Bend 4 - HV bend
Bend 5 - VH bend

Along x-axis

Bend 1

Along y-axis

Along z-axis

Inlet
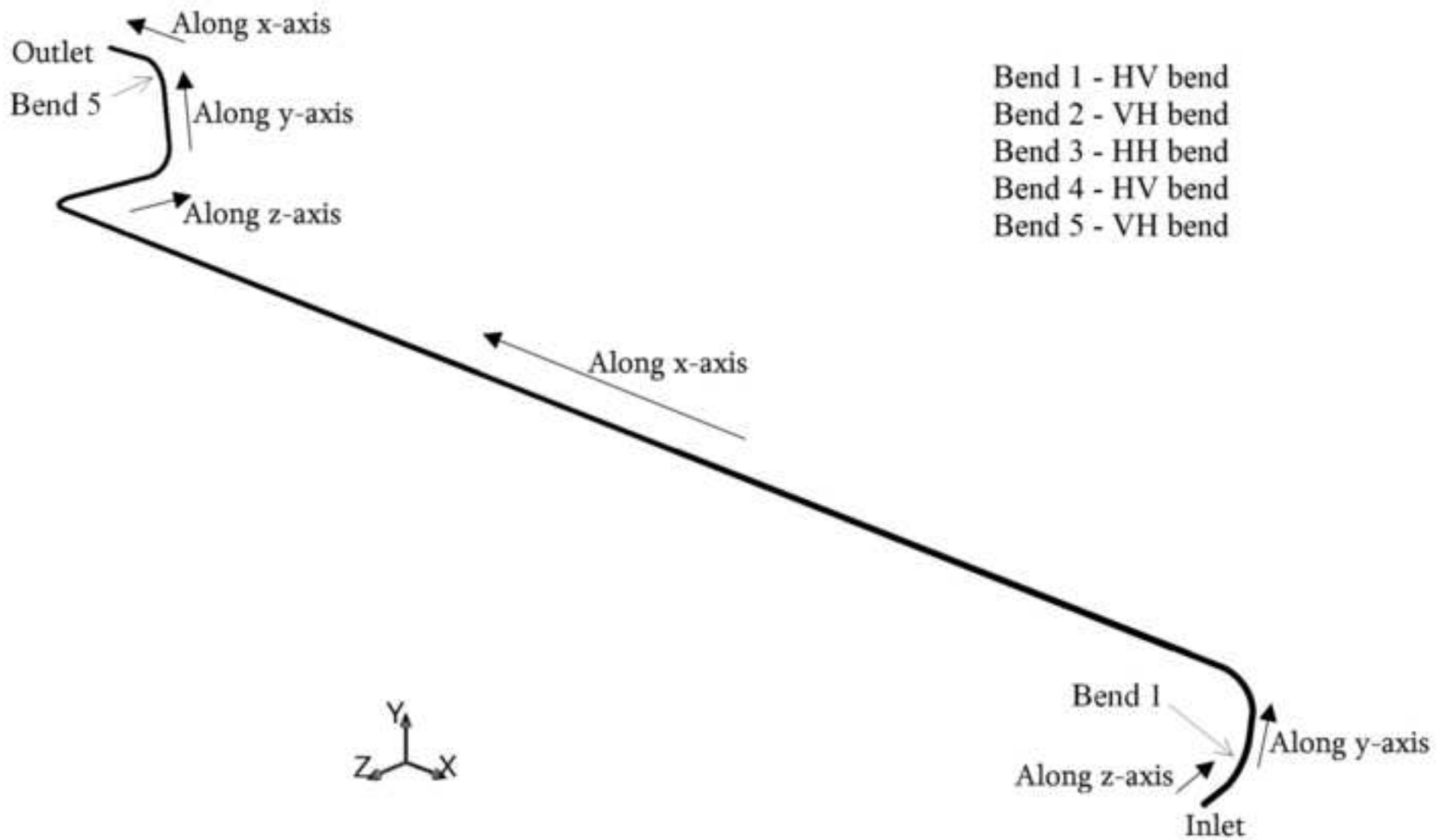
Figure 2
Click here to download high resolution image

11.4d horizontal

318.6d horizontal

8.2d horizontal   7.0d horizontal

14.6d vertical

4.5d vertical

R 2.5m

Ø 0.3556m

8.35m   118.3m

13.1m

5m

10.2m

6.6m
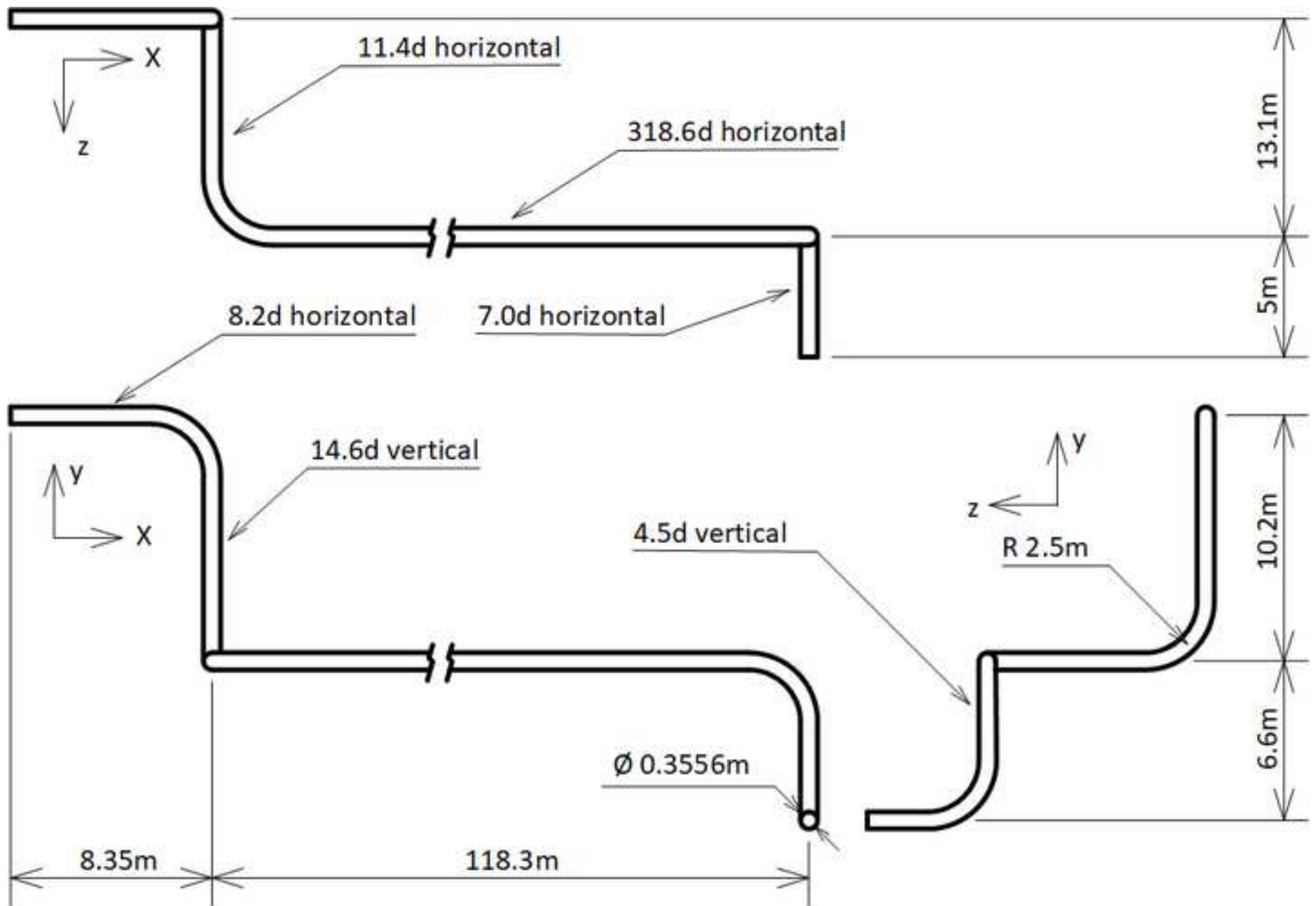
Figure 3
[Click here to download high resolution image](#)
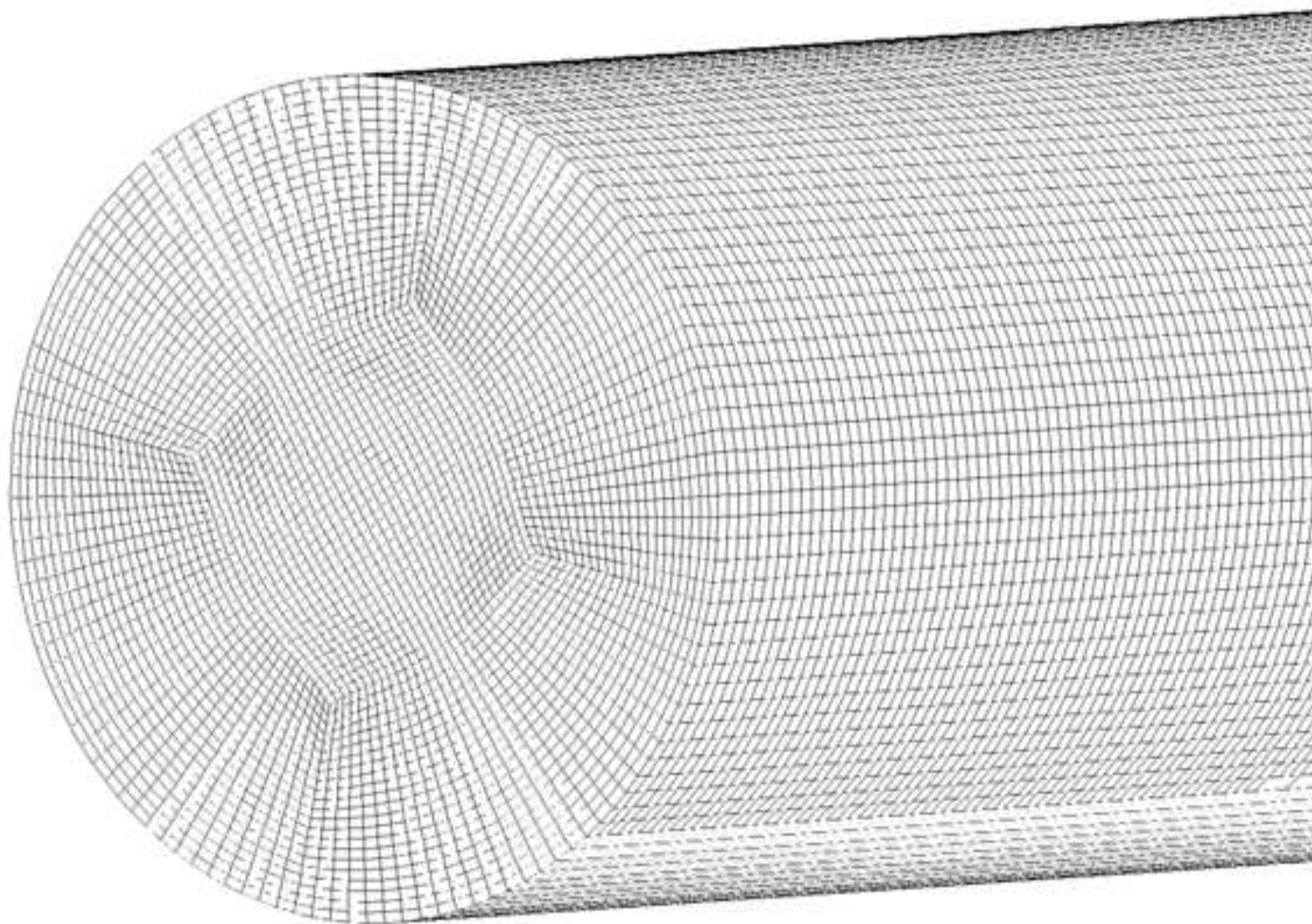
Figure 4
Click here to download high resolution image
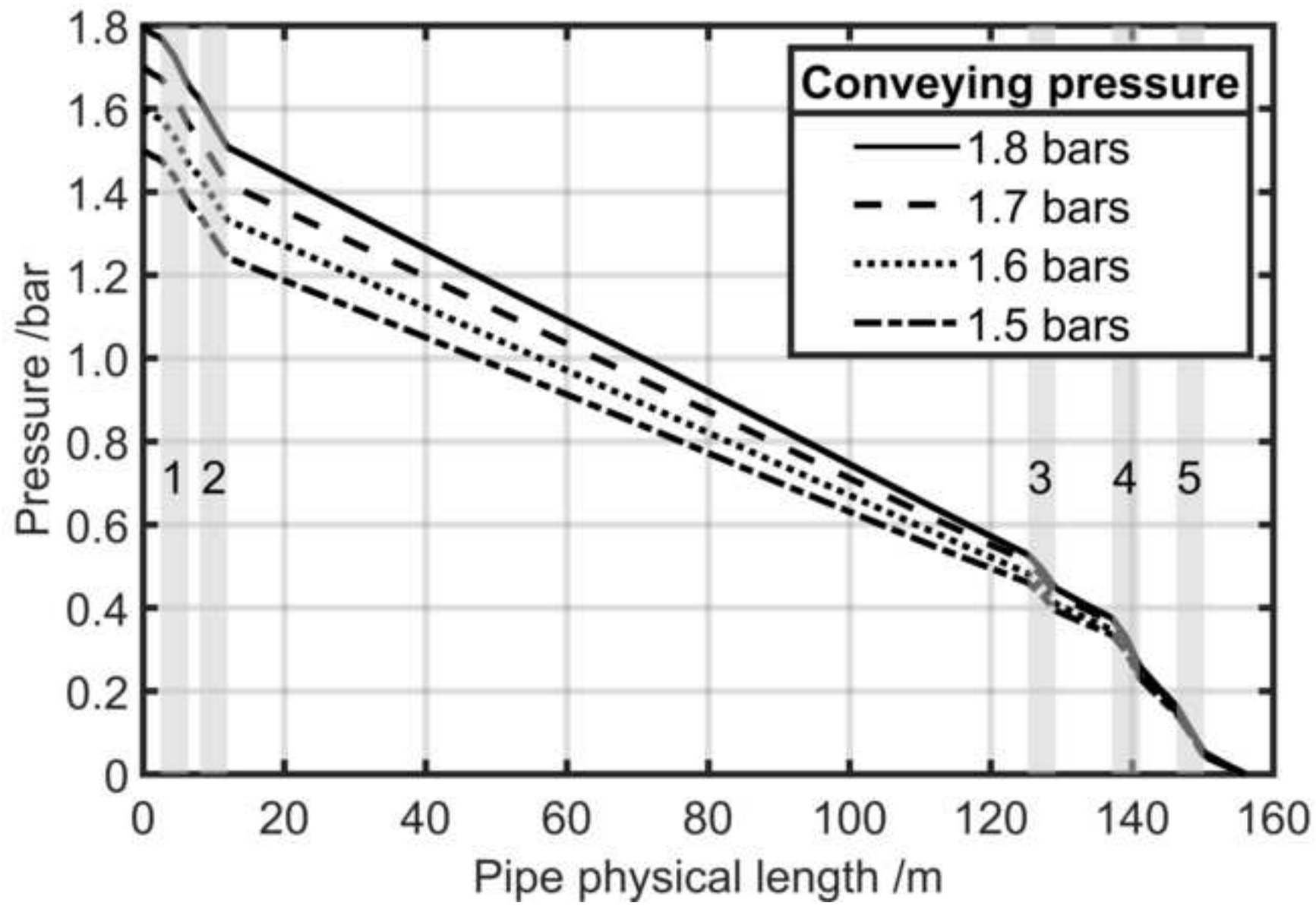
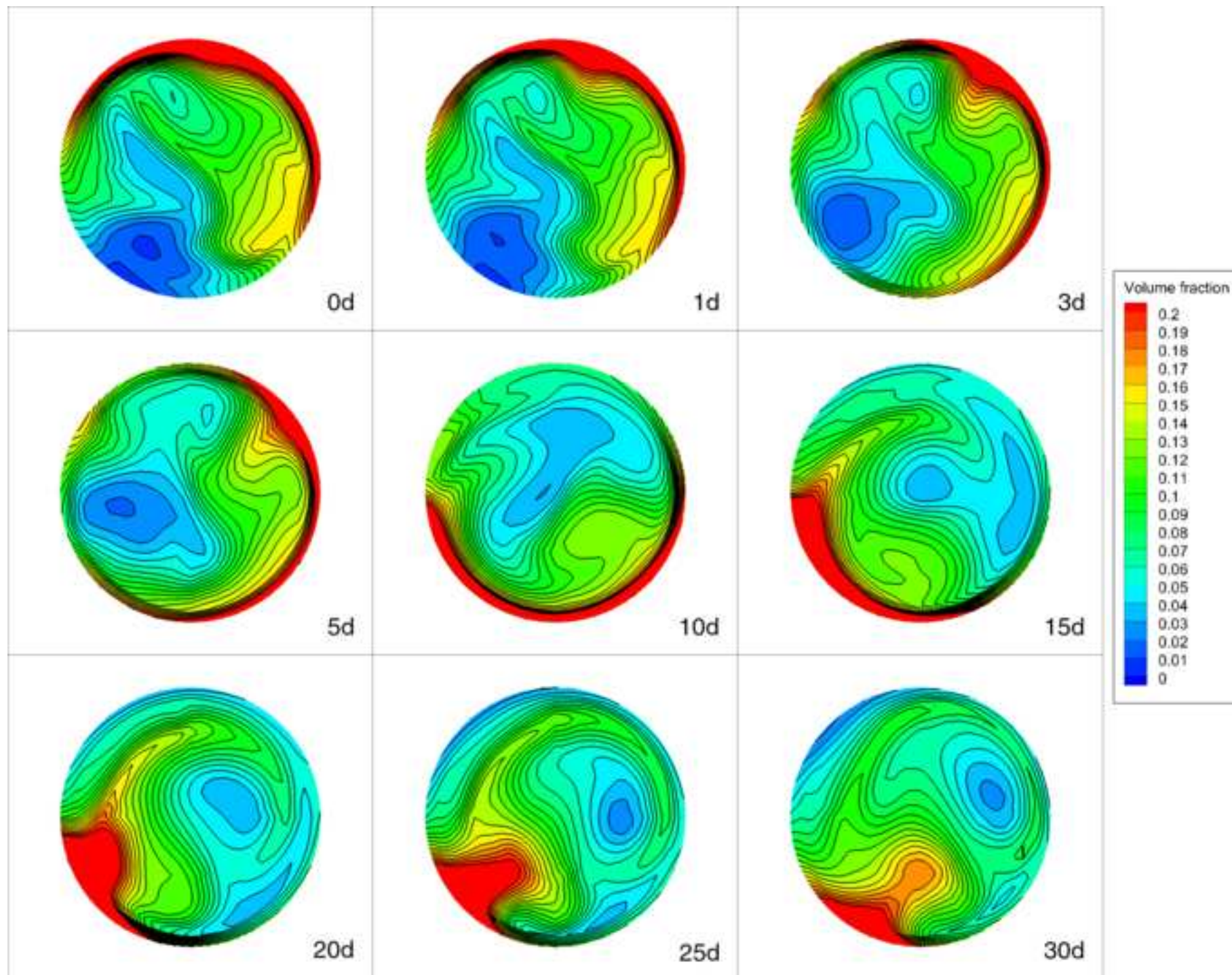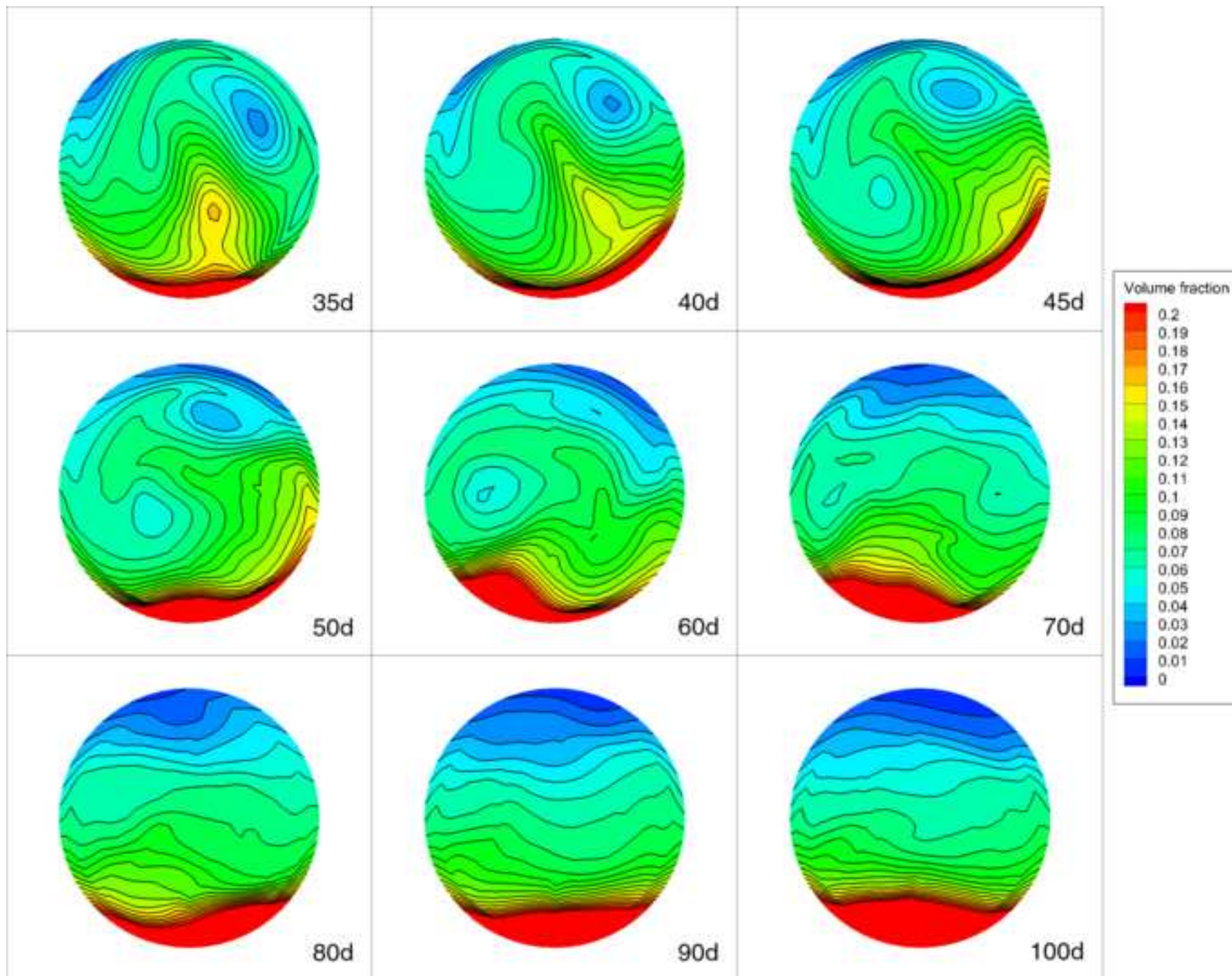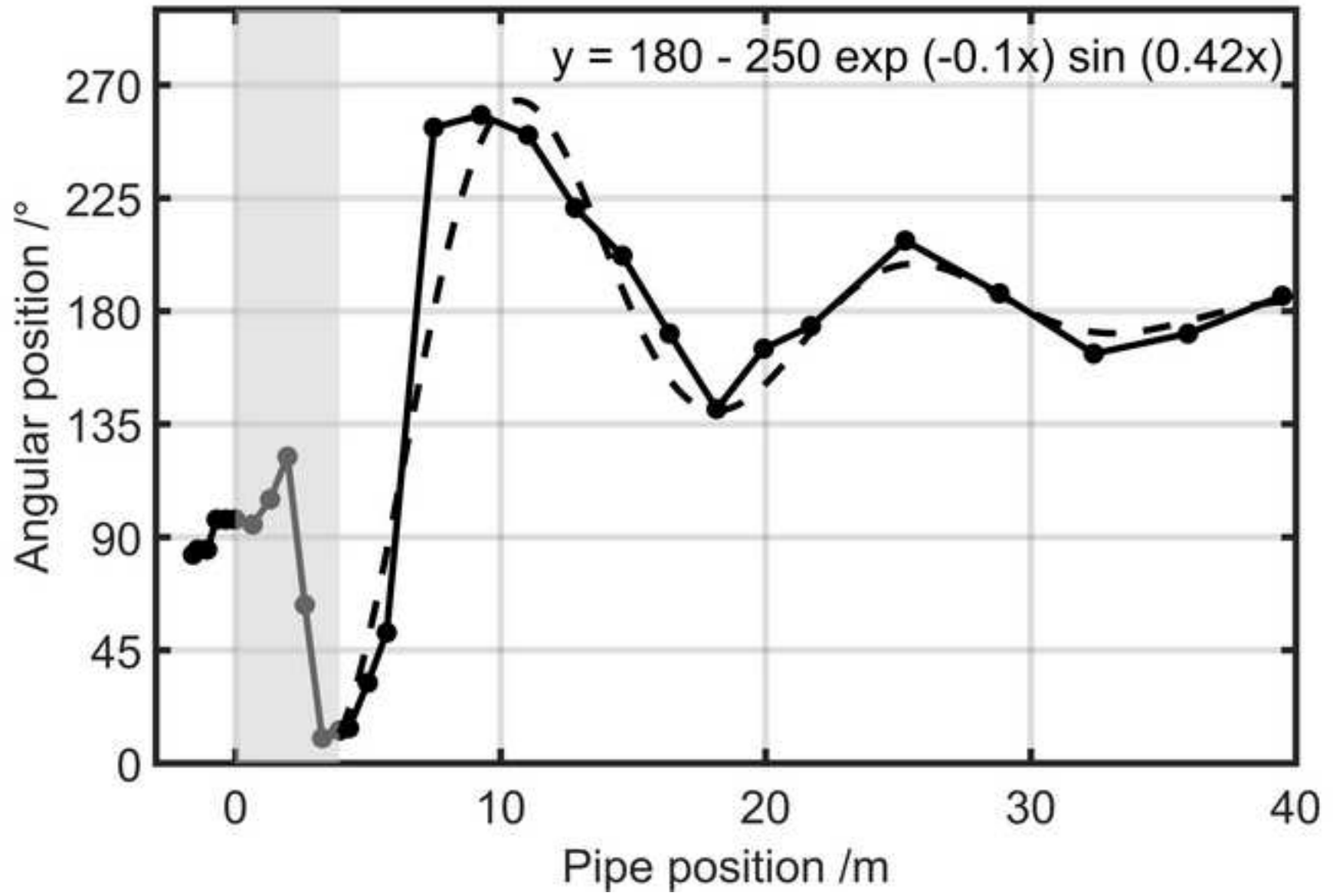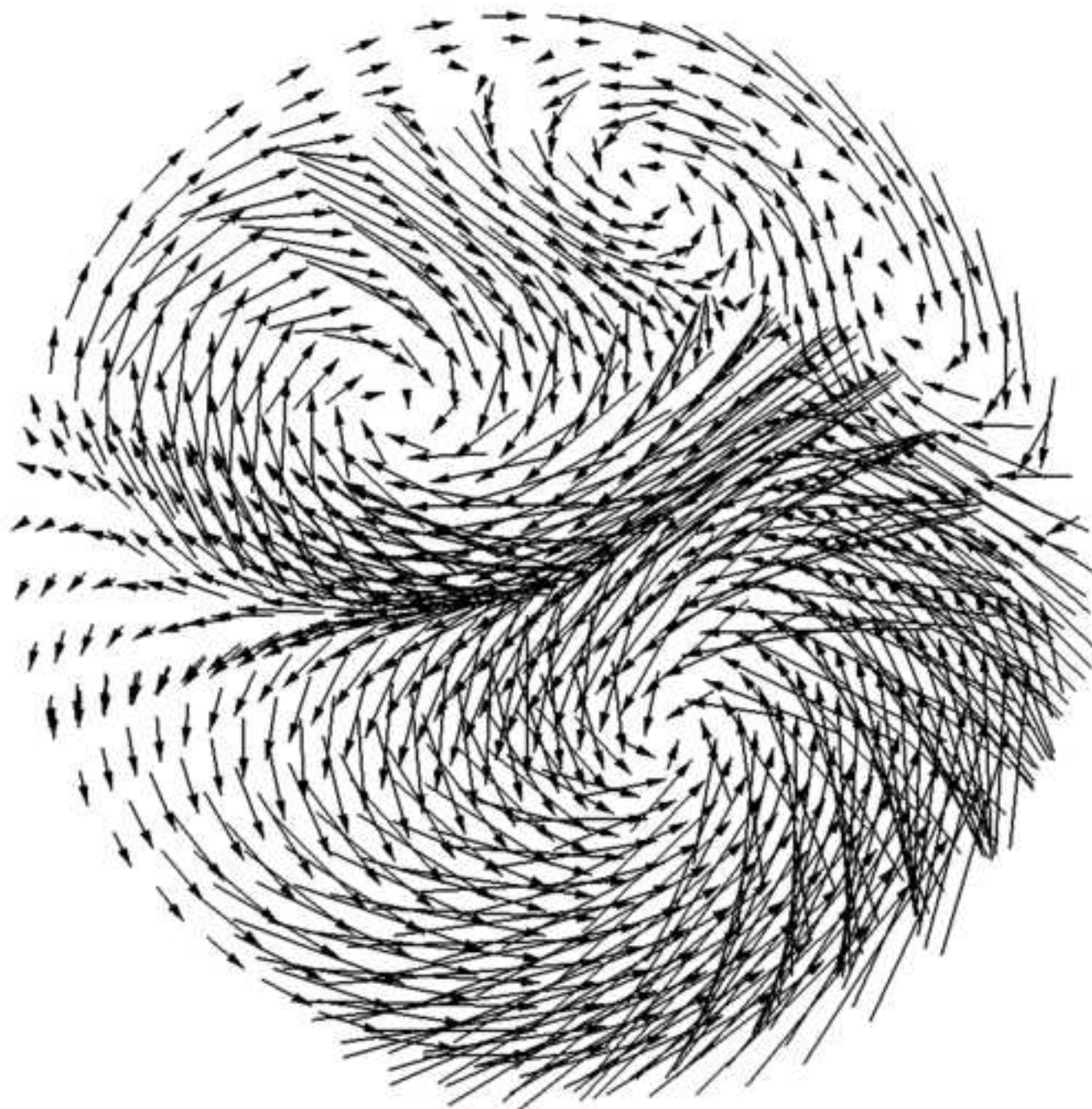**Figure 5**
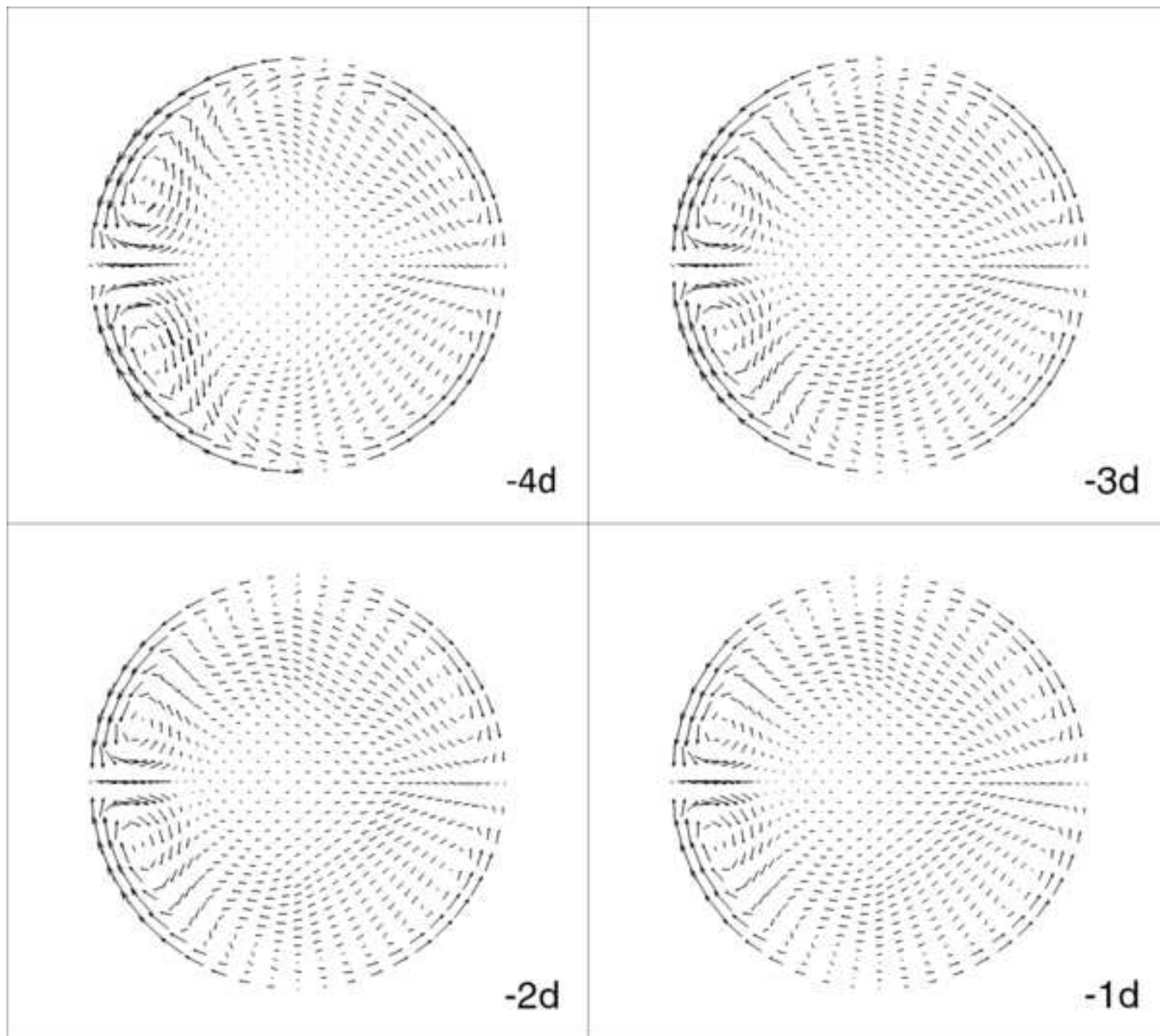**Click here to download high resolution image**
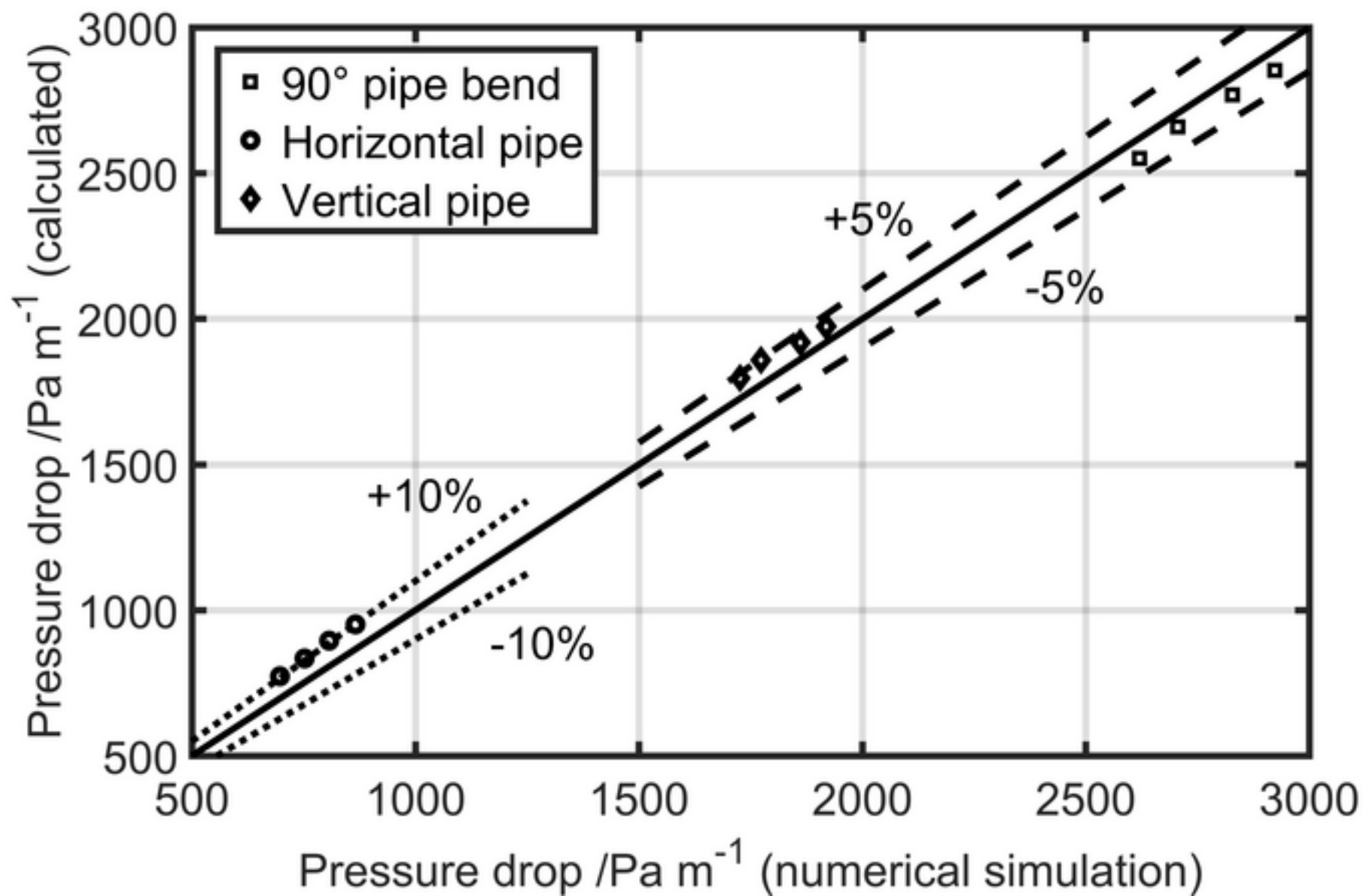
Figure 5

50d

40d

30d

20d

10d

0d

Pipe diameters (d)
After the bend
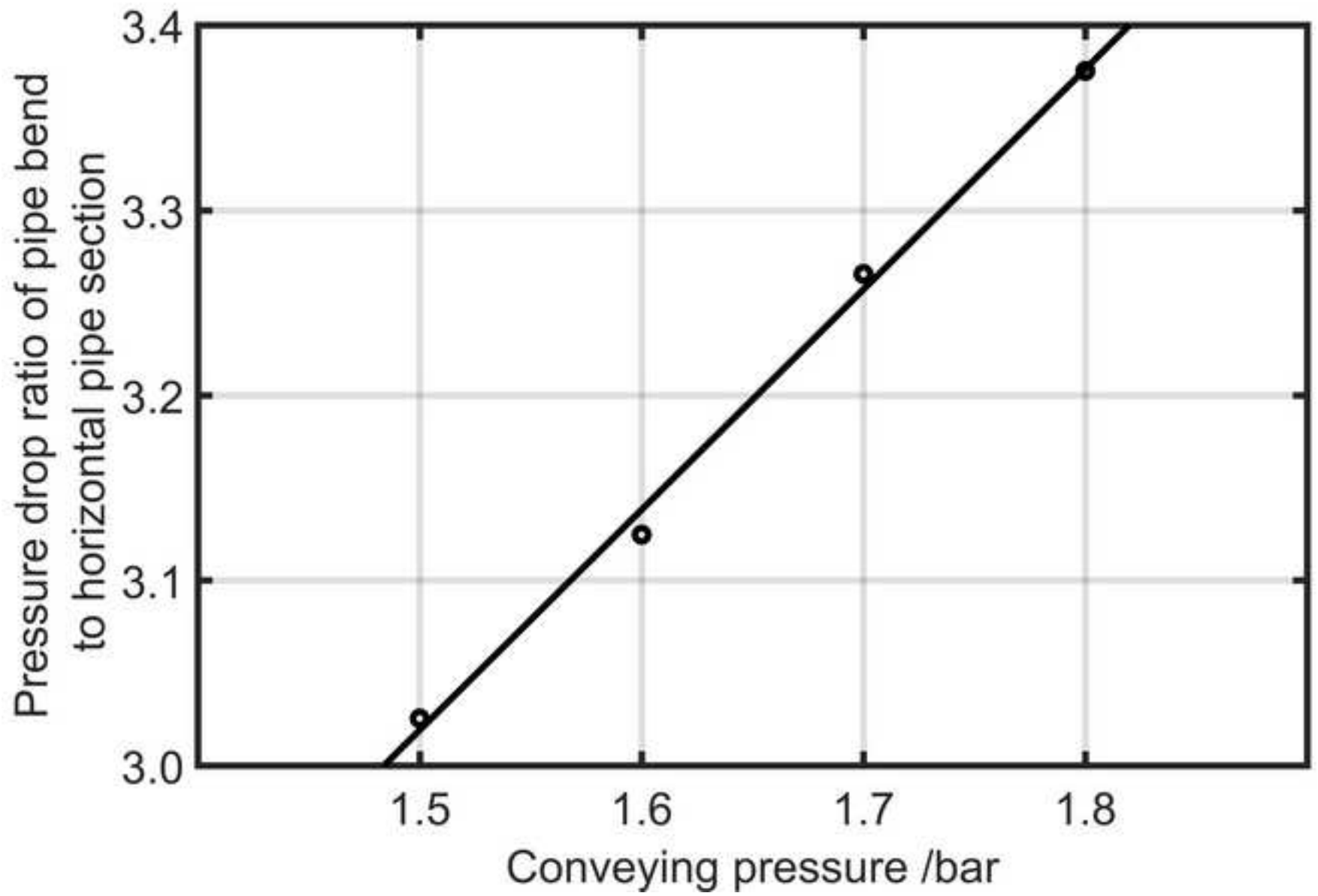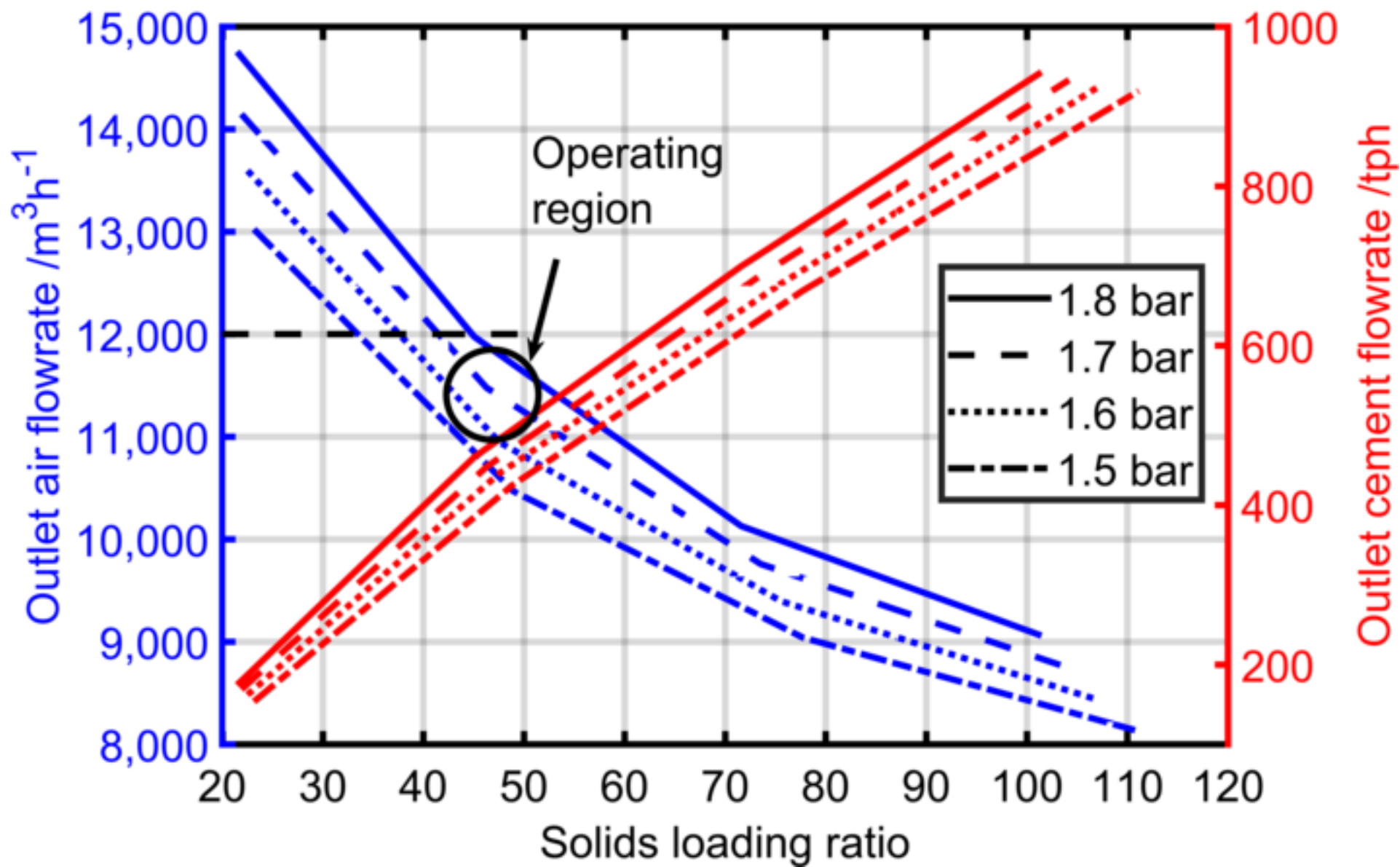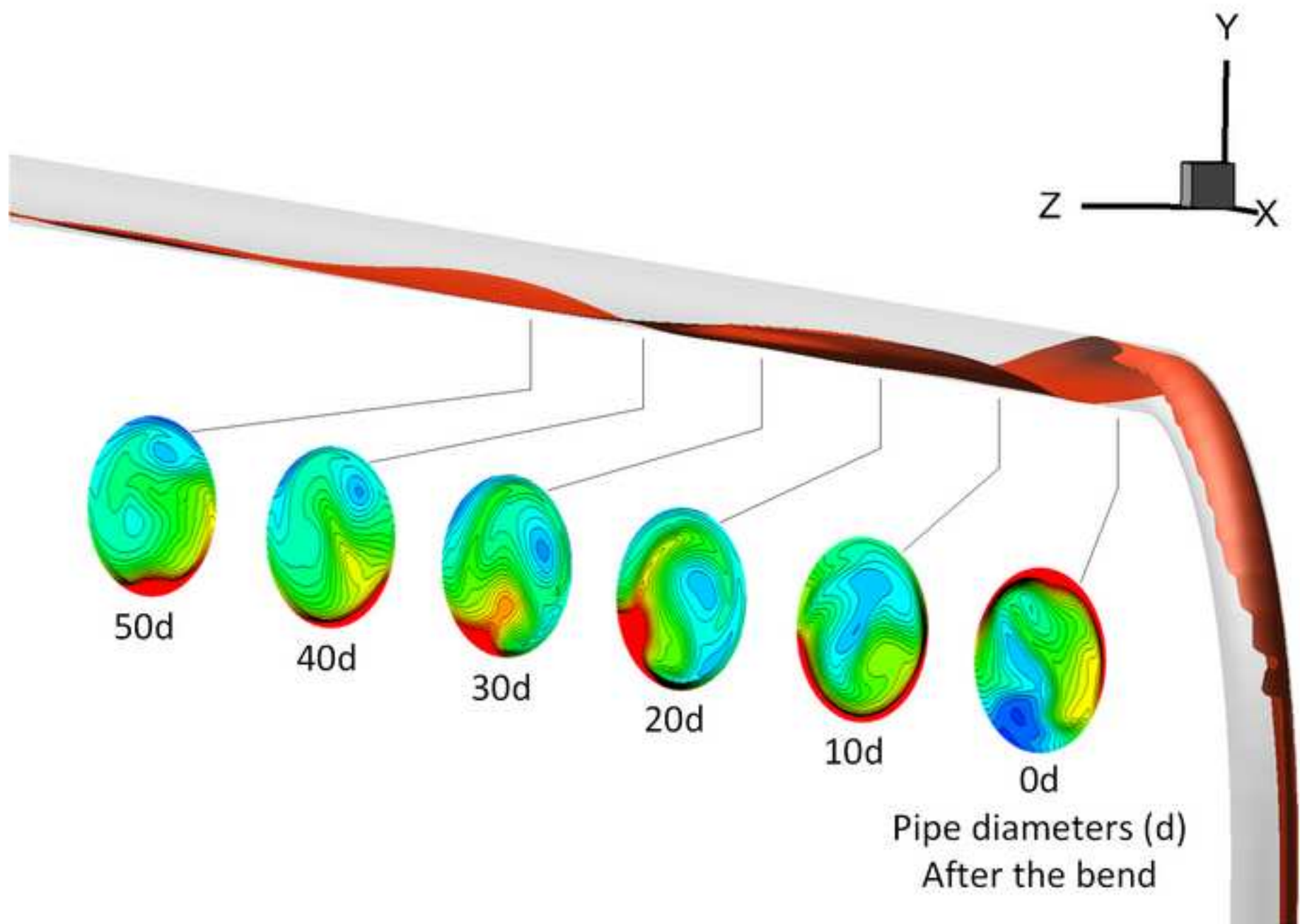
Figure 9
Click here to download high resolution image
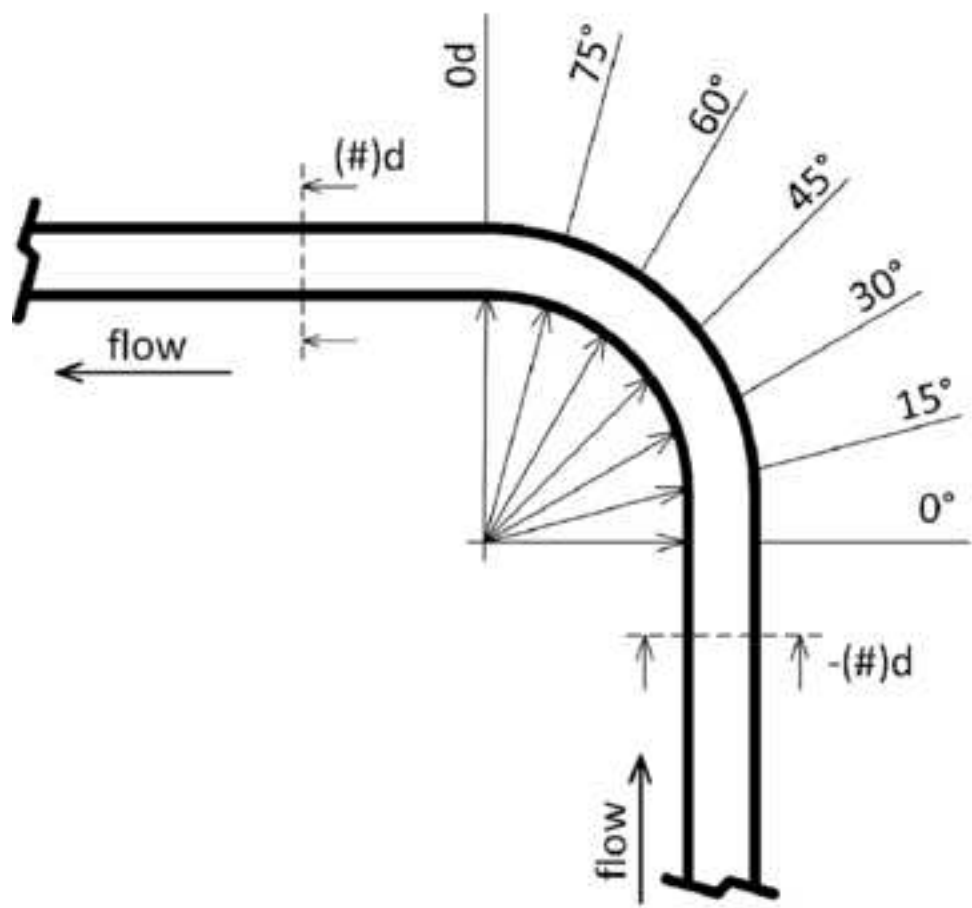
(a)

(b)
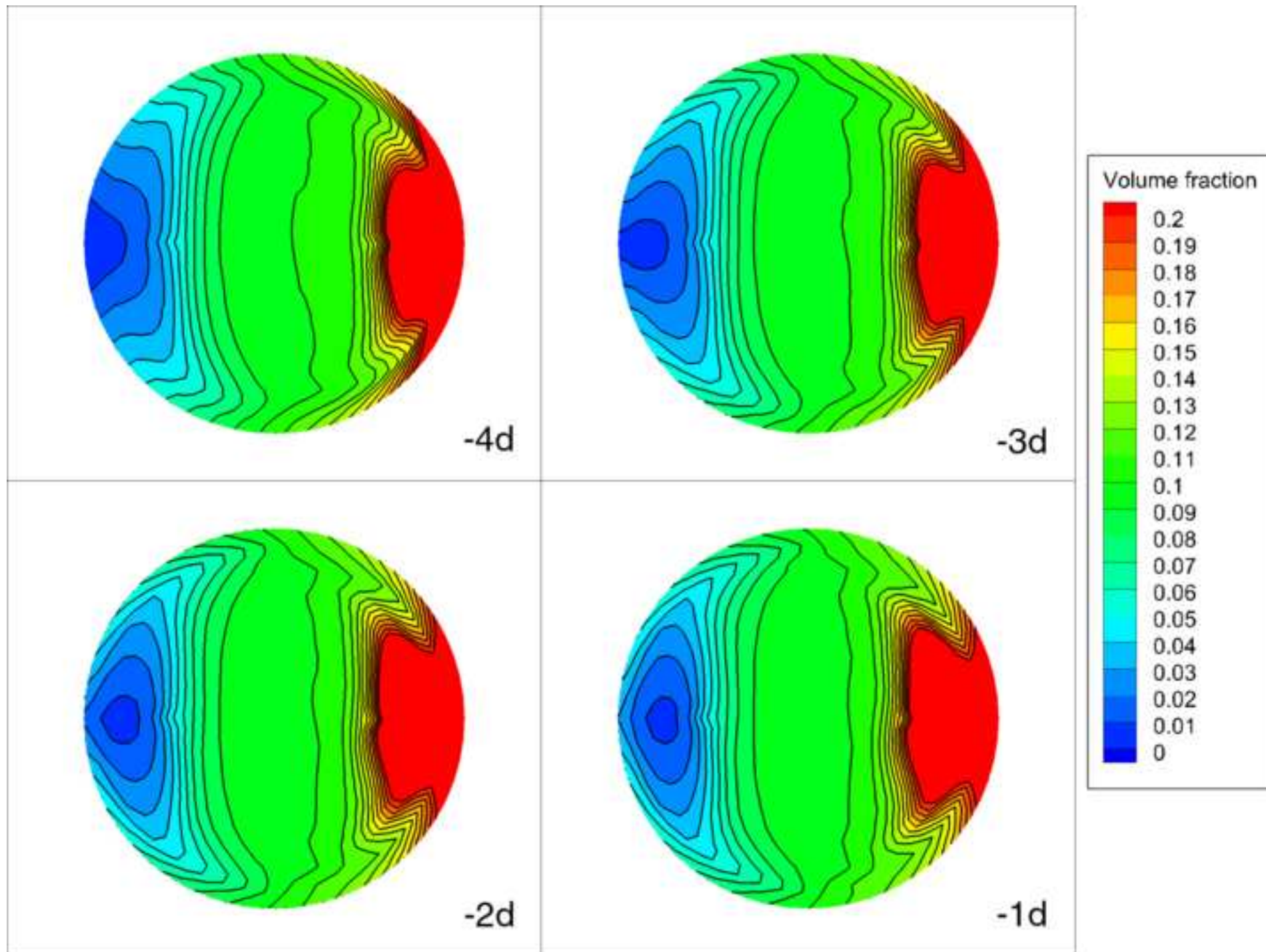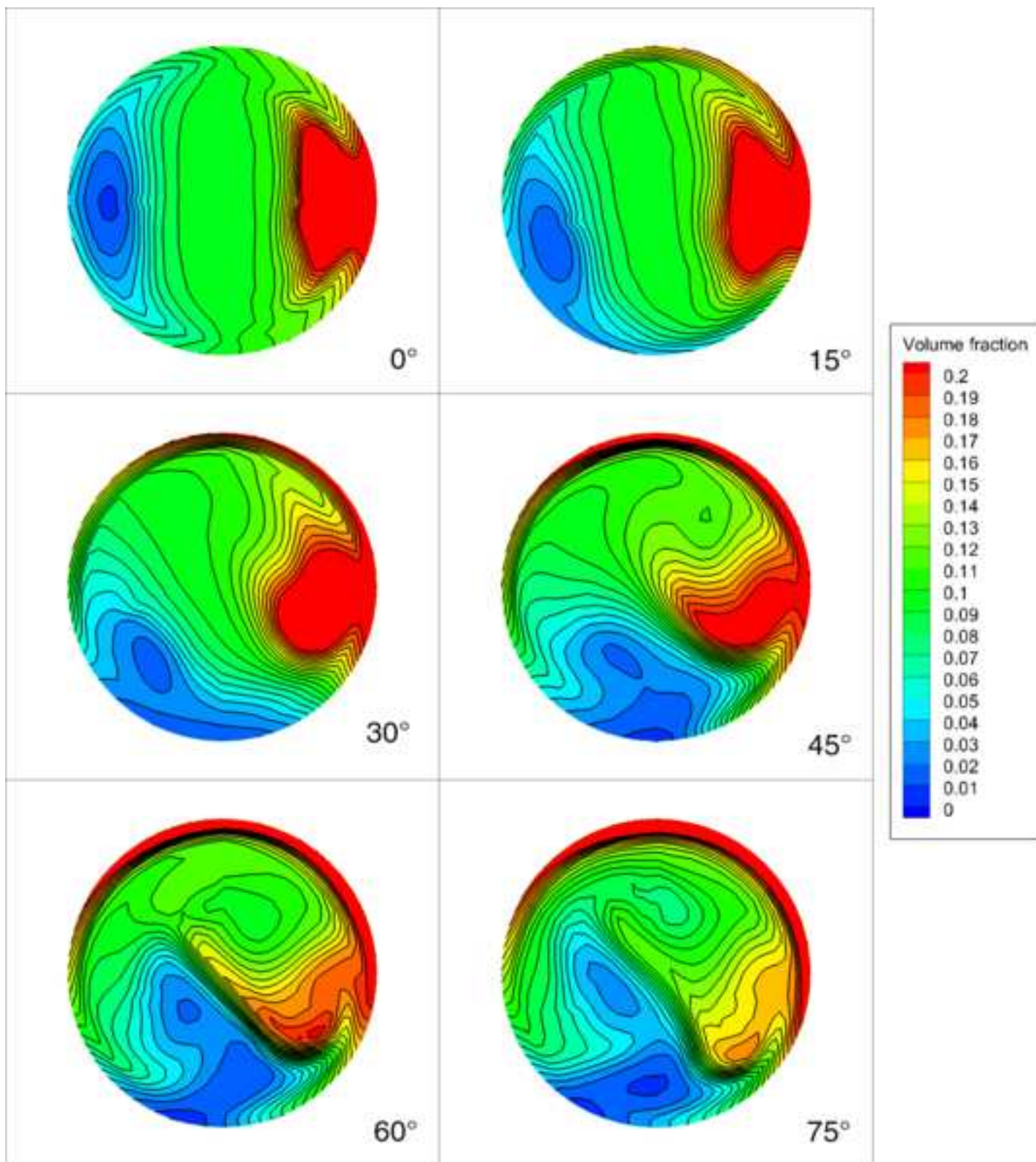
Figure 12(a)
Click here to download high resolution image

0d	1d	3d
5d	10d	15d
20d	25d	30d

Volume fraction

0.2
0.19
0.18
0.17
0.16
0.15
0.14
0.13
0.12
0.11
0.1
0.09
0.08
0.07
0.06
0.05
0.04
0.03
0.02
0.01
0

Figure 12(b)
Click here to download high resolution image

Volume fraction
0.2
0.19
0.18
0.17
0.16
0.15
0.14
0.13
0.12
0.11
0.1
0.09
0.08
0.07
0.06
0.05
0.04
0.03
0.02
0.01
0

Figure 13

$y = 180 - 250 \exp(-0.1x) \sin(0.42x)$

Figure 14
Click here to download high resolution image

-4d

-3d

-2d

-1d

Figure 16
[Click here to download high resolution image](#)

0°

15°

30°

45°

60°

75°
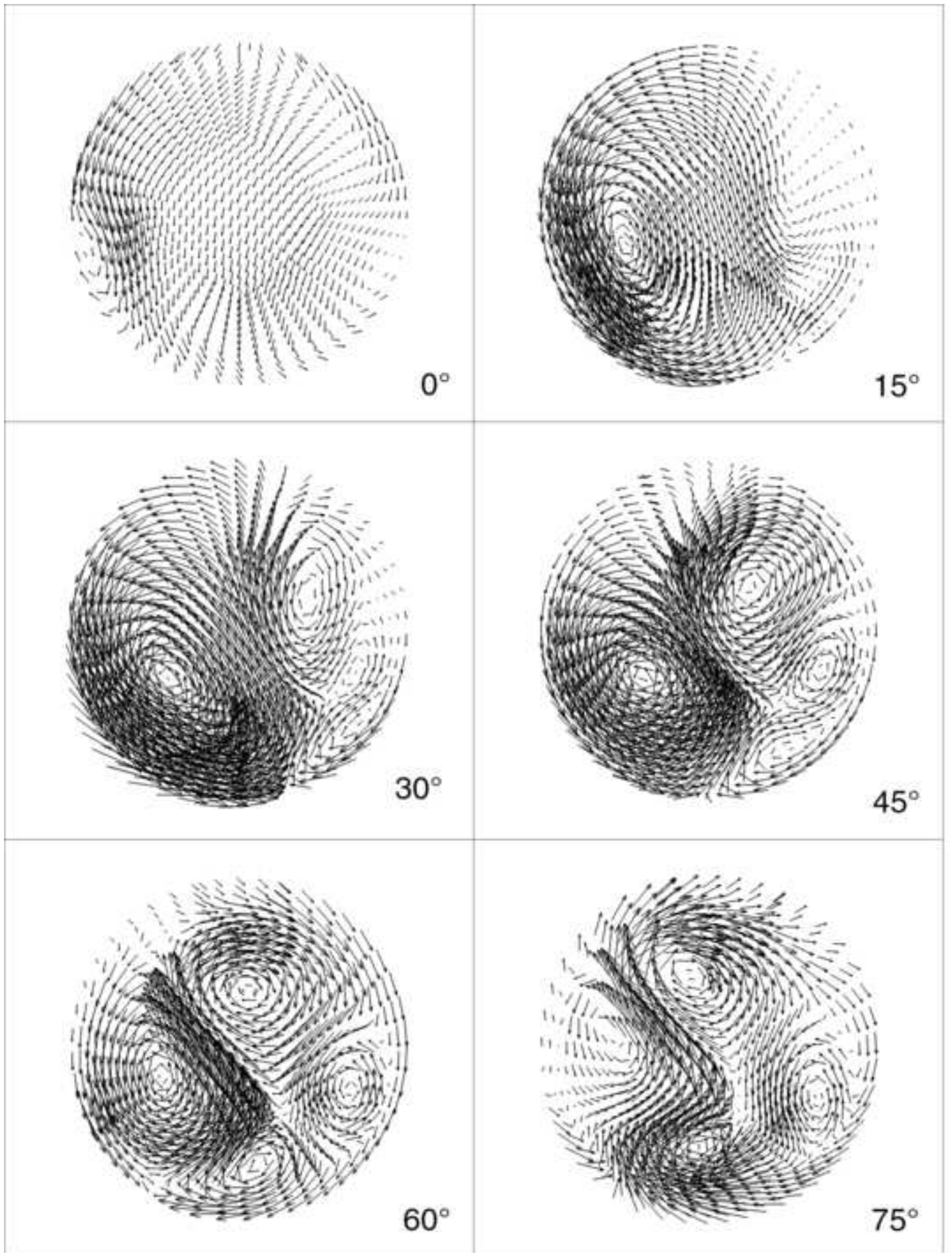
Figure 17(a)
Click here to download high resolution image

0d

1d

3d

5d

10d

15d

20d

25d

30d
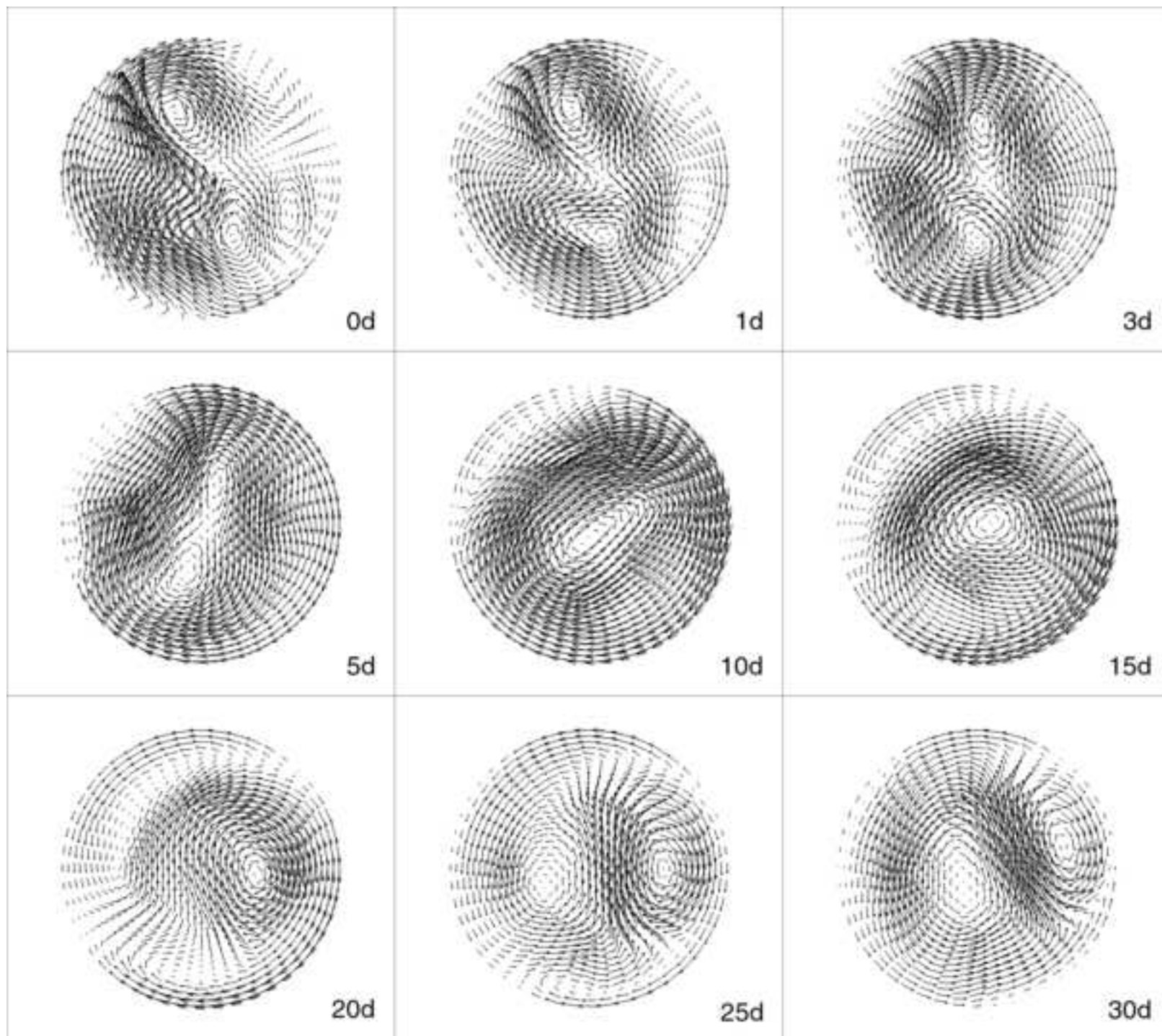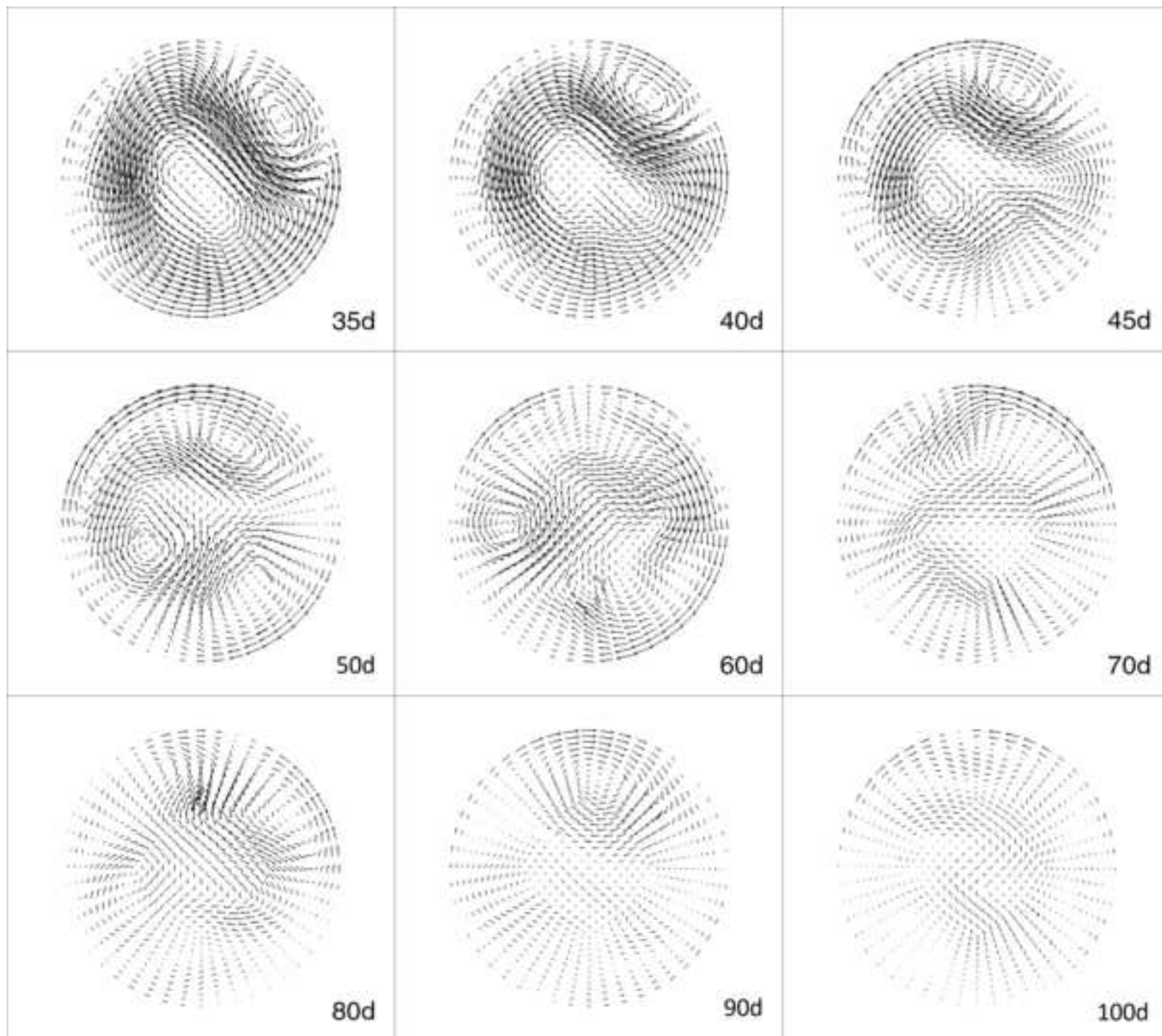
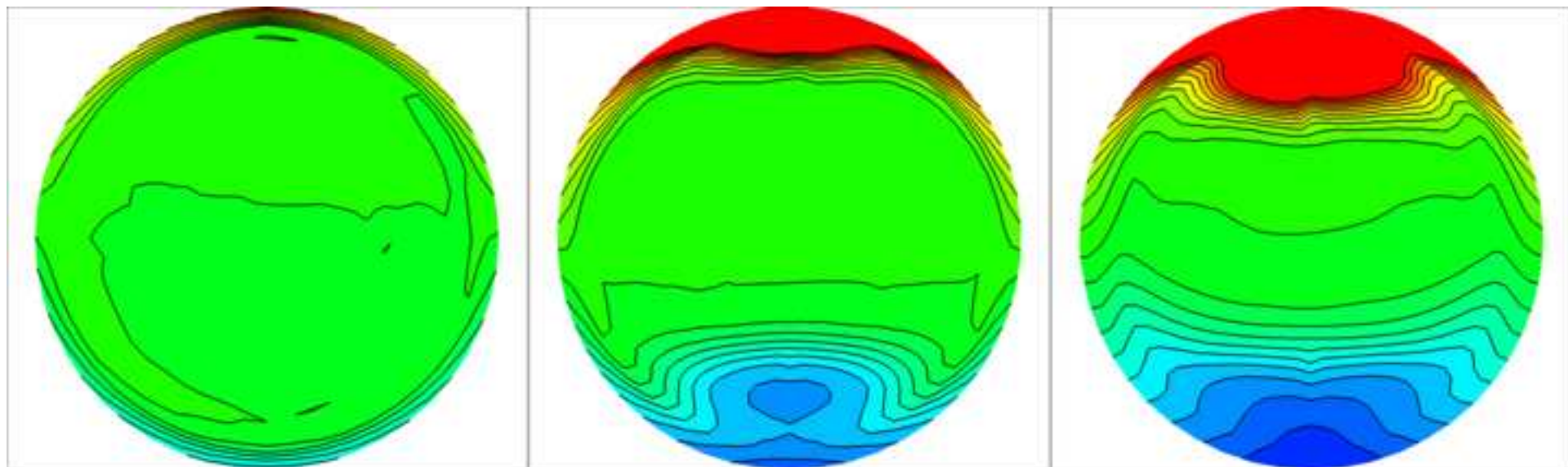**Figure 17(b)**

Figure 18
Click here to download high resolution image

0 deg   45 deg   90 deg

Figure 19
Click here to download high resolution image

Bend 2

Bend 3

Bend 4

Bend 5

0 deg   45 deg   90 deg